ADVANCED THEORY AND SIMULATIONS
www.advtheorysimul.com

Understanding the Origin of the Particularly Small and Anisotropic Thermal Expansion of MOF-74

*Tomas Kamencek, Benedikt Schrode, Roland Resel, Raffaele Ricco, and Egbert Zojer**

Metal–organic frameworks often display large positive or negative thermal expansion coefficients. MOF-74, a material envisioned for many applications, shows a different behavior. Temperature-dependent X-ray diffraction reveals particularly small negative (positive) thermal expansion coefficients perpendicular (parallel) to the hexagonally arranged pores. These trends are explained by combining density-functional theory calculations with the Grüneisen theory of thermal expansion, which allows tracing back thermal expansion to contributions of individual phonons. On the macroscopic level, the small thermal expansion coefficients arise from compensation effects caused by the large coupling between perpendicular stress and strain and by the small magnitudes of the mean Grüneisen tensor elements, $\langle\gamma\rangle$. These provide information on how strains impact phonon frequencies. To understand the small value of $\langle\gamma\rangle$, the individual mode contributions are analyzed using the corresponding atomic motions. This reveals that only the lowest frequency modes up to ≈3 THz provide non-negligible contributions, such that $\langle\gamma\rangle$ drops sharply at higher temperatures. These considerations reveal, how the details of the anharmonic properties of specific phonon bands determine the magnitude and sign of thermal expansion in a prototypical material like MOF-74. Beyond that, the authors also discuss, how the choice of the theoretical methodology impacts the obtained results.

1. Introduction

Metal–organic frameworks (MOFs[1–4]) are a booming class of porous materials with an enormous accessible surface area, often amounting to several thousand square meters per gram.[5–7] Therefore, MOFs have a high potential for applications such as gas storage,[8–10] catalysis,[11–13] and gas separation.[14,15] They are also used in various functional devices.[16–20] In many of those applications, the thermal expansion of MOFs is a highly relevant property.[21,22] For example, it determines the thermal mismatch (and the resulting thermal stresses)[23–26] for heteroepitaxial growth processes,[27,28] or the change of the pore volume with temperature. Therefore, considerable efforts have been dedicated to studying thermal expansion in MOFs by means of both simulations and experiments. Experimental studies have, for example, focused on isoreticular MOFs (IRMOFs),[29–32] DUTs,[30,33] HKUST-1,[30,34–36] MOFs containing paddle-wheel secondary building units (SBUs),[22,30,37] UiOs,[30] FMOF-1,[38] MCF-34,[39] ZIF-8,[40] MOF-74,[41] and others.[42–51] These experimental investigations are complemented by simulations, for example, for IRMOFs,[21,26,52–55] DUTs,[56] HKUST-1,[26] paddle-wheel MOFs,[30] MOF-74,[57] and others.[26,56,58,59] For the meaning of the acronyms, we refer the reader to the respective references, as the detailed chemical nature of the above systems is not of immediate relevance for the following discussion. What is rather relevant is that MOFs described in literature often show rather sizable linear and volumetric thermal expansion coefficients (either positive or negative). This is shown in **Figure 1**. Notably, these thermal expansion coefficients in MOFs are usually much larger than for many common non-porous materials.[53,60,61] As a result, computational and experimental studies of thermal expansion in MOFs are typically concerned with explaining the origins of the large positive thermal expansion, PTE, and negative thermal expansion, NTE, coefficients.

For archetypical MOFs such as IRMOFs and HKUST-1, several relevant mechanisms and factors of influence have been identified. These are related to optical[29,31,32,34,55,56] or acoustic[52] phonons, and potentially also to adsorbates,[54] where a correct treatment of anharmonicities in the potential energy surface has been shown to be crucial.[62] These considerations emphasize that studying thermal expansion is also an important first step

T. Kamencek, R. Resel, E. Zojer
Institute of Solid State Physics
Graz University of Technology
NAWI Graz, Petersgasse 16, Graz 8010, Austria
E-mail: egbert.zojer@tugraz.at
T. Kamencek, R. Ricco
Institute of Physical and Theoretical Chemistry
Graz University of Technology
NAWI Graz, Stremayrgasse 9, Graz 8010, Austria
B. Schrode
Anton Paar GmbH
Anton-Paar-Straße 20, Graz 8054, Austria
R. Ricco
School of Engineering and Technology
Asian Institute of Technology
58 Moo 9, Khlong Luang, Pathum Thani 12120, Thailand

The ORCID identification number(s) for the author(s) of this article can be found under https://doi.org/10.1002/adts.202200031

DOI: 10.1002/adts.202200031

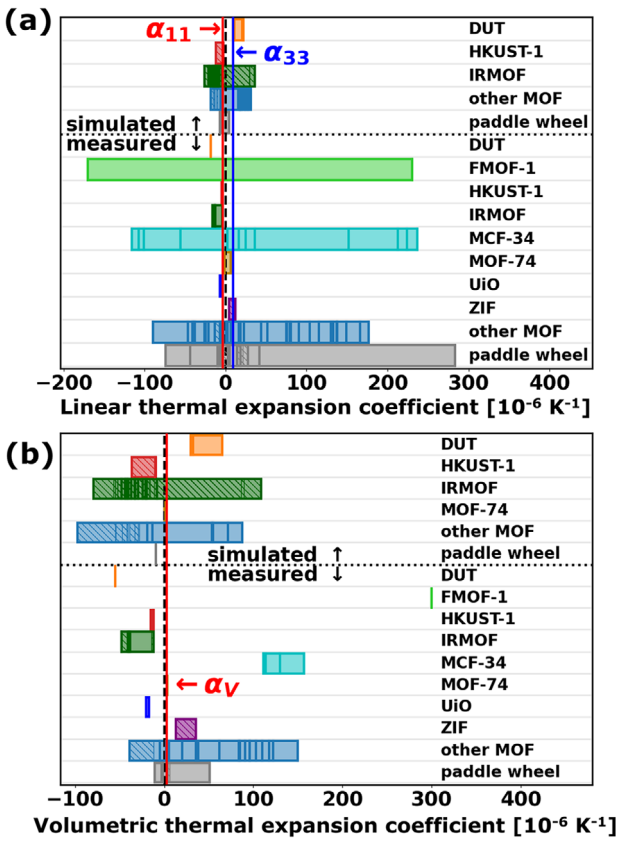

Figure 1. a) Linear and b) volumetric thermal expansion coefficients for several MOFs reported in literature based on modeling (IRMOFs,[21,26,52–55] DUTs,[56] HKUST-1,[26] paddle-wheel MOFs,[30] MOF-74,[57] and others[26,56,58,59]) or experimental studies (IRMOFs,[29–32] DUTs,[30,33] HKUST-1,[30,34–36] paddle-wheel MOFs,[22,30,37] UiOs,[30] FMOF-1,[38] MCF-34,[39] ZIF-8,[40] MOF-74,[41] and others[42–51]). The colossal thermal expansion coefficients of FMOF-1 in nitrogen atmosphere (-1.3×10^{-2} and 1.2×10^{-2} in the *ab*-plane and in *c*-direction,[38] respectively) are not shown to enhance the visibility of the remaining MOF systems. The horizontal bars are drawn from the minimum to the maximum reported value of the respective MOF family, with vertical lines and hatched areas inside the colored bars representing individual values and ranges of thermal expansion values (e.g., upon varying linker lengths, adsorbates, topology, etc.) They have been taken from different papers and are reported for different crystallographic directions. The vertical red and blue lines in panel (a) denote the calculated linear thermal expansion coefficients (from the present work) for (activated) MOF-74(Zn) at 300 K in *x*(*y*)- (α_{11}) and *z*-direction (α_{33}) at 300 K, respectively. The red line in panel (b) indicates the low volumetric thermal expansion coefficient, α_V, (at 300 K) calculated in this work.

toward understanding the anharmonic character of phonon modes in MOFs, which is relevant also for other processes like thermal conduction.[62–67] Particularly relevant quantities in this context are the so-called mode Grüneisen parameters, which describe the relative changes of the frequencies of individual phonon modes with the unit-cell volume (or the applied strain). These mode Grüneisen parameters are directly connected to higher-order force constants beyond the harmonic approximation.[68–70] In this context, non-cubic MOFs are particularly interesting, as they allow studying the effects of anisotropic anharmonicities.

A practically relevant example of such an anisotropic system is zinc-based MOF-74,[71,72] which is in the focus of the present study. MOF-74 has been employed in different applications including colorimetric sensing,[73] adsorption chillers,[74] drug delivery,[75] and gas storage for, e.g., CO_2[76] and H_2.[9,77] When considering the thermal expansion of MOFs, MOF-74 shows comparably small linear expansion coefficients. Thus, MOF-74 can rather be defined as a low-thermal-expansion material (LTE). In fact, its volumetric thermal expansion coefficient is particularly low at relevant temperatures, such that it lies in a similar range as certain ceramics often referred to as zero-thermal-expansion materials (ZTE).[78–83] In contrast to classical ZTE materials, in which the vanishingly small volumetric thermal expansion coefficients are caused by small linear coefficients in all spatial directions, in MOF-74 the particularly small volumetric expansion is the consequence of cancellation effects. They are caused by the combination of the PTE and NTE behavior in different spatial directions, as will be discussed in more detail below. Thus, in the following, we will exclusively refer to MOF-74 as an LTE material. Its LTE behavior is consistent with existing "rough" theoretical estimates[57] (relying on a mixture of density-functional theory and force field calculations disregarding the anisotropy of the material). It is also in line with previous experimental findings for magnesium-based MOF-74,[41] which at room temperature suggest a positive thermal expansion coefficient of $\approx 6.7 \times 10^{-6}$ K^{-1} along the pore axis and a negative thermal expansion coefficient of $\approx -1.5 \times 10^{-6}$ K^{-1} perpendicular to it. This raises the question, which mechanisms are responsible for the LTE behavior of MOF-74. The structure of MOF-74 comprises hexagonal channels with 1D metal-oxide SBUs located at the corners of the hexagons and organic linkers forming the walls in between (see **Figure 2**). The physical properties of MOF-74 distinctly differ for directions along its pores and perpendicular to them. This is not surprising, considering that for the former the characteristics of the inorganic SBUs dominate, while for the latter the organic linkers play a much more prominent role.[57,64,84] The fundamental reasons for the LTE behavior of MOF-74, however, remain unclear. The present study aims at changing that by identifying the origins of the low thermal expansion of pristine zinc-based MOF-74 at an atomistic level, with a particular focus on the material's anisotropy. To this end, we combine diffraction studies with theoretical considerations based on state-of-the-art ab initio simulations within the framework of the Grüneisen theory of thermal expansion.[85] This approach (in contrast to, for example, molecular dynamics simulations) allows a phonon-resolved analysis of the situation such that one can assign to each phonon mode a quantitative contribution to the thermal expansion tensor. By analyzing the frequency ranges and wave vector-dependencies of the phonon bands with particularly relevant contributions, one is then able to identify trends and to systematically unravel the mechanisms behind the observed behavior. On more methodological grounds, we will also critically assess the performance of various approaches within the quasi-harmonic approximation (QHA) (mostly within the Supporting Information).[70,86,87] Moreover, we will emphasize the delicateness of modeling effects that are as small as the thermal expansion of MOF-74 by comparing the results obtained with the supposedly very similar PBE[88,89] and PBEsol[90,91] functionals.

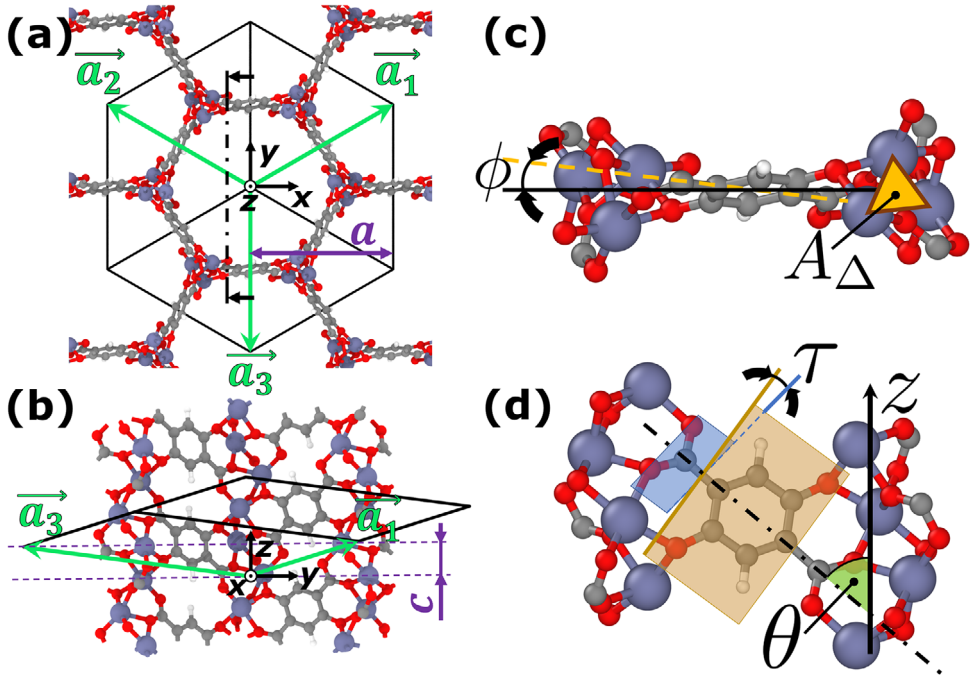

Figure 2. a) Top and b) side view of the rhombohedral crystal structure of MOF-74 illustrating the two independent lattice parameters, a and c. The projections of the lattice vectors ($\vec{a_n}$ with $n = 1,2,3$) are shown as colored arrows. The lattice parameter a is drawn in a way that it corresponds to the Cartesian x-component of lattice vector $\vec{a_1}$. The primitive Cartesian lattice vectors are constructed from a and c in the following way: $\vec{a_1} = [a, a/\sqrt{3}, c]$, $\vec{a_2} = [a, -a/\sqrt{3}, c]$, and $\vec{a_3} = [0, -2a/\sqrt{3}, c]$. The vertical dash-dotted line denotes the plane at which the structure is cut for the side view shown in panel (b), as seen in the direction of the black arrows. b) Side view of the crystal structure illustrating the second independent lattice parameter c as the Cartesian z-component of all three lattice vectors. Atomic color coding: H: white, C: grey, O: red, and Zn: purple. c,d) Details of the structure of MOF-74 in which the most relevant geometric descriptors are shown: the cross-sectional area of the nodes, A_Δ, defined by the projection of the centers of the Zn^{2+} ions onto the xy-plane, the inclination angle, ϕ, between the edges of the nominal pore wall (i.e., the hypothetic regular hexagon connecting the centers of the nodes; black horizontal line in panel (c)) and the projections of the linker backbones onto the xy-plane, the dihedral angle, τ, between the COO^- group of the linker and the phenylene ring, and the polar linker tilt angle, θ, between the node axes (parallel to the z-axis) and the long molecular axes of the linkers (dash-dotted line).

The article is structured as follows: first, we briefly discuss the crystal structure of MOF-74 and provide the relevant synthetic, experimental, and theoretical details including a short summary of the Grüneisen theory of thermal expansion. Subsequently, the experimental results and their evaluation are discussed, followed by a detailed (phonon-resolved) analysis of the governing anharmonicities and contributions to the thermal expansion. This is concluded by a short discussion of methodological aspects. While the experiments yield observable thermal expansion values and represent a basis for the calculations, the simulations provide the desired mechanistic insights.

2. Experimental Section

2.1. The Crystal Structure of MOF-74

The primitive crystallographic unit cell of MOF-74 with its three lattice vectors, $\vec{a_n}$ ($n \in \{1,2,3\}$), is shown in Figure 2. Although MOF-74 could be synthesized with a number of different metal ions,[92–98] with linkers consisting of more than one benzene ring,[72] and with modified docking groups,[99] whenever it is referred to MOF-74 in the remainder of this article it means pristine and activated MOF-74 based on Zn^{2+} ions connected by 2,5-dihydroxy-terephthalate linkers. The structure of MOF-74 belongs to space group $R\bar{3}$ (international number 148) and has a rhombohedral (trigonal) Bravais lattice. Unlike many other MOFs, MOF-74 formes 1D extended pores arranged in a honeycomb-like lattice. This results in a distinct structural anisotropy. Accordingly, also the metal (oxide) nodes consist of (infinitely extended) quasi-1D arrangements of Zn and O atoms. Note that in the activated (pristine) state, the Zn atoms in MOF-74 are undercoordinated, but still exhibit an (approximately) octahedral coordination geometry. Due to its rhombohedral symmetry, the lattice has two independent lattice parameters, a and c (from which the primitive lattice vectors are constructed as explained in the caption of Figure 2): The distance between the metal atoms along the z-axis in the nodes equals c, while the pore diameter in the xy-plane (i.e., the distance between two opposite corners of the hexagon) equals $4a/3$, as illustrated in Figure 2a. Because of this distinct structural anisotropy, also the materials properties are expected to strongly depend on the crystallographic directions. This circumstance offers ideal conditions to separately study anharmonic effects in the z-direction and in directions within the xy-plane. These can then be associated with the nodes (dominating in z-direction) and the linkers of the MOF (relevant in the xy-plane).

In order to gain mechanistic insight and to qualitatively rationalize the signs of the mode Grüneisen tensor components in Section 3, it was analyzed, how certain geometric descriptors are impacted by the different phonon modes. This strategy was similar to the one used in ref. [84], where such descriptors quantified the structural changes upon applying stress to the unit cell of MOF-74. The geometric descriptors include: the cross-sectional area of the nodes, A_{Δ}, defined by the projection of the centers of the Zn^{2+} ions onto the xy-plane, the inclination angle, ϕ, between the edges of the nominal pore wall (i.e., the hypothetic regular hexagon connecting the centers of the nodes) and the projections of the linker backbones onto the xy-plane, the dihedral angle, τ, between the COO^{-} group of the linker and the benzene ring, and the polar linker tilt angle, θ, between the node axes and the long molecular axes of the linkers. The mentioned descriptors are schematically depicted in Figure 2c,d. For more details about their definition see Section S10, Supporting Information and ref. [84].

2.2. Experimental Methods

The studied MOF-74 powder samples were obtained following the solvothermal synthesis protocols of ref. [100]. Temperature-dependent X-ray diffraction (XRD) was used to study the pristine MOF. Prior to the XRD measurements, the samples were activated directly in the in situ temperature chamber (TTK 600 from Anton Paar) by heating them to 300 °C in vacuum (10^{-2} mbar) and keeping them at that temperature for 15 min. After the activation, the temperature was decreased stepwise, and X-ray diffractograms were recorded in Bragg–Brentano geometry using a PANalytical Empyrean diffractometer with a Cu radiation source, a primary Soller slit with a divergence angle of 0.02 rad, a divergence slit of 0.25°, a secondary 0.02 rad Soller slit, an anti-scatter slit with an angle of 0.25°, and an X'Celerator detector. To avoid a decrease in intensity, no additional monochromator was used, and to improve the thermal equilibration of the sample, a waiting time of up to 30 min was introduced between the time, when the internal sensor of the heating stage reached the set point temperature and when the XRD measurements were started. Furthermore, at each temperature the sample was aligned with respect to the X-ray beam to account for the thermal expansion of the setup.

The experimental results were analyzed using Bayesian probability theory to achieve meaningful results.[101] This was necessary due to the very minor change of the structural parameters with temperature combined with average peak widths of 0.19°. Additionally, a statistical analysis also allowed to take into account uncertainties in the determination of the sample temperature. Finally, employing a probabilistic approach also enabled the determination of estimators for the uncertainty of the calculated results. A mathematically rigorous description of the employed approach can be found in Section S2, Supporting Information.

2.3. Theoretical Methods

To generate the desired level of atomistic insight, ab initio calculations were carried out in the framework of density functional theory (DFT),[102,103] employing the VASP[104–107] code (version 5.4.4). Technically, these simulations were performed at 0 K (i.e., unlike in a molecular dynamics run, the atoms were kept fixed at their positions), but the temperature dependence of the phonon frequencies and occupations and, thus, the thermal expansion tensor were accounted for, as described below. The exchange-correlation contributions were described via the PBEsol functional[90,91] in combination with the D3-BJ[108,109] a posteriori van der Waals correction. Additionally, tests employing the PBE functional[88,89] are contained in Sections S4, S5, Supporting Information. Here it should not be concealed that they yield a different sign for the thermal expansion coefficient of the lattice parameter c compared to employing PBEsol. This is primarily a consequence of the fact that in MOF-74 one is dealing with overall very small effects. As discussed briefly at the end of the Section 3 and in more detail in Section S5, Supporting Information, the origin of the observation can be traced back to qualitatively different, small changes of certain geometric descriptors with strain or phonon displacements that are observed for the two functionals. In this context, it should, however, be stressed that PBEsol is supposed to yield more accurate structural properties[90,91,110] and thermal expansion coefficients[70,111,112] for solids (with smaller charge density gradients). Thus, the vast majority of studies calculating thermal expansion coefficients within DFT typically relies on the PBEsol functional. Moreover, only PBEsol yields results that are consistent with the most probable outcome of the authors' experiments (see below) and with the neutron diffraction data of the Mg-analogue of MOF-74 in ref. [41]. Finally, as again shown in Section S3, Supporting Information, only with PBEsol qualitatively consistent trends between the most sophisticated calculations performed within the QHA and in the framework of the Grüneisen Theory of thermal expansion are obtained. Therefore, in the main manuscript the results of the PBEsol calculations are primarily focused on.

In the simulations, the crystal structure of the primitive unit cell (including lattice parameters) was first optimized to maximum residual forces below 1 meV $Å^{-1}$ using a $3 \times 3 \times 3$ k-mesh and a plane wave energy cutoff of 1000 eV for the optimization of the lattice constants and atomic positions. The elastic tensor and the compliance tensor were calculated according to the approach described in ref. [84] and in Section S4, Supporting Information, keeping the particularly high cutoff energy of 1000 eV, following the convergence studies shown in ref. [84]. Based on careful and extensive convergence tests discussed in Section S4, Supporting Information, a $1 \times 1 \times 3$ supercell of the conventional unit cell was employed for the subsequent phonon calculations. This hexagonal supercell contained nine primitive unit cells, as shown in Section S4.3, Supporting Information. As a consequence of the supercell size, its electronic structure had to be sampled only at the Γ-point to achieve convergence. An advantage of the conventional unit cell is that it allows to probe the interatomic force constants more efficiently in real space, since a corresponding $1 \times 1 \times 3$ supercell has approximately the same unit-cell extents along all directions. For the phonon calculations, due to the enormous system size of the supercells, the plane wave energy cutoff was reduced to 800 eV (which required a reoptimization of the atomic positions with this cutoff, which was done for the primitive unit cell with a $3 \times 3 \times 3$ k-mesh, see Section S4, Supporting Information). In all simulations, an energy convergence criterion of

10^{-8} eV for the self-consistency cycle, and a Gaussian smearing of the electronic states with a width of 0.05 eV were employed.

For the chosen way of incorporating temperature (entropy) effects into the thermodynamic considerations, one first requires the phonon band structures of the material. For those phonon band structure calculations, the phonopy[113] package (version 2.9.1) was used and the first Brillouin zone was sampled with a $20 \times 20 \times 20$ mesh of phonon wave vectors, $\boldsymbol{q}$, when calculating thermodynamic properties.

When following the evolution of the above-defined geometrical descriptors as a function of strain, two distinct situations were considered : i) uniaxial strain parallel to the pore (i.e., in z-direction) and ii) isotropic strain perpendicular to the pore (i.e., in the xy-plane). The latter is a more realistic scenario than applying uniaxial strain in either x- or y-direction because in the absence of external stresses, the thermal strain is isotropic in the xy-plane for a system with rhombohedral symmetry.

For the visualization of the crystal structure and of phonon modes, as well as for recording the corresponding animations, the Ovito package (version 3.3.1) was used.[114]

2.3.1. Anisotropic Thermal Expansion

One possible strategy for computing the thermal expansion tensor of a material would be to calculate the temperature-dependent (non-equilibrium) total Gibbs free enthalpy, G, (i.e., the contributions from electrons, phonons, and the elastic energy due to externally applied stress[115–117]) for various combinations of lattice constants. Then, at each temperature, one could identify the set of lattice constants, which minimize the free enthalpy at each temperature to determine the thermal expansion coefficients. This minimization is typically achieved by fitting an analytical function (such as the well-known equations of state of Birch,[118] Murnaghan,[119] or Vinet et al.[120]) to the free enthalpy-versus-lattice constants data and taking the minimum of the chosen model function (which are systematically compared in refs. [121, 122]). This approach is commonly referred to as the QHA.[70,86,87] Several flavors of this approach were applied to the case of MOF-74, as discussed in Section S3, Supporting Information, including the procedure followed by George et al.[123] for several organic crystals and the approach by Holec et al.[124] who incorporated the anisotropy at a more sophisticated level. Overall, the results of the common QHA-based approaches sensitively depended on fitting and minimizing Gibbs free enthalpies with respect to finite strains. For thermal expansion coefficients as small as the ones encountered in MOF-74, the changes in the free enthalpy became, however, so small that fitting a model function and finding the associated minima (relying on well-established routines of the numpy,[125] scipy,[126] or scikit-learn[127] packages) became numerically stable only for applied strains much larger than the thermal strains suggested by the authors' experiments. This means, for realistically small strains, the QHA fitting and minimization became highly inaccurate, while for unrealistically large strains, the results obtained within the QHA overestimated the thermal expansion especially for the lattice parameter c (see the extensive discussion in Section S3, Supporting Information).

In the case of MOF-74, the authors, therefore, resorted to the Grüneisen theory of thermal expansion,[85] which is a more direct quasi-harmonic approach to access the thermal expansion tensor without the need to fit free enthalpies.[70,85] In combination with the PBEsol functional this approach yielded results in rather good qualitative and also quantitative agreement with the experimental observations shown below.

The central quantity in the Grüneisen theory is the mode Grüneisen tensor, γ_{ij}^{λ} (Cartesian components $i, j \in \{1 = x, 2 = y, 3 = z\}$). It is defined as the (negative) first derivative of the phonon frequency, ω, with respect to the components of the strain tensor, ϵ_{ij}, for each phonon mode, λ (as indicated by super- and subscripts):[68,70,128]

$$\gamma_{ij}^{\lambda} = -\frac{1}{\omega_{\lambda}} \frac{\partial \omega_{\lambda}}{\partial \epsilon_{ij}} \tag{1}$$

In practice, the partial derivatives in Equation (1) were determined based on the derivatives of the dynamical matrix (at 0 K), which were approximated by finite differences (see Section S3.7, Supporting Information). Hence, it was necessary to calculate the dynamical matrix for the equilibrium unit cell at 0 K as well as the dynamical matrices for suitably strained cells. In order to improve the numerical accuracy in the calculation of the finite differences, a more accurate fourth-order finite difference scheme was implemented, as detailed in Section S3.7, Supporting Information, where also the choice of 10^{-3} for the strain step size is briefly motivated.

Based on the mode Grüneisen tensors, one can calculate the temperature-dependent mean Grüneisen tensor, $\langle \gamma_{ij} \rangle$, employing Equation (2). It can be interpreted as the average value of γ_{ij}^{λ} weighted with the phonon mode contributions to the heat capacity (in the grand-canonical ensemble), $c_{\mathrm{v}}{}^{\lambda}$, at a specific temperature, T:

$$\langle \gamma_{ij} \rangle (T) = \frac{\sum_{\lambda} c_{\mathrm{v}}^{\lambda}(T)\, \gamma_{ij}^{\lambda}}{\sum_{\lambda} c_{\mathrm{v}}^{\lambda}(T)} \tag{2}$$

Note that the temperature dependence of $\langle \gamma_{ij} \rangle$ arises solely from the temperature dependence of the mode contributions to the heat capacity, while, at the same time, the (0 K-) mode Grüneisen tensors is used.

Finally, the thermal expansion tensor, α_{ij}, is directly related to $\langle \gamma_{ij} \rangle$, to the compliance tensor, S_{ijkl}, and to the phonon heat capacity per volume, C_{V}/V, according to Equation (3).[70]

$$\alpha_{ij} = \frac{C_{\mathrm{V}}}{V} \sum_{kl} S_{ijkl} \langle \gamma_{kl} \rangle \tag{3}$$

A derivation of this equation is contained in Section S3.7, Supporting Information. In contrast to the situation in cubic materials, the entire compliance tensor rather than the (inverse) bulk modulus enters Equation (3), such that the crystal anisotropy is considered when (thermal) stresses lead to (anisotropic) strains. In contrast to QHA-based approaches (see Section S3, Supporting Information), one cannot readily predict the temperature dependence of the compliance tensor with the Grüneisen theory. In fact, considering the variation of S_{ijkl} with temperature would drastically increase the complexity of the calculations, making them prohibitively expensive for sophisticated ab initio methods.

To avoid resorting to a lower level of theory, the authors, thus, used the compliance tensor obtained from precise DFT-calculations of the 0 K-structure. Consequently, the temperature dependence of the thermal expansion tensor was approximated to arise solely from the numerator of Equation (2) (as the denominator cancels with the heat capacity in Equation (3)). Neglecting the temperature dependence of the compliance tensor is a drawback of the Grüneisen theory of thermal expansion, but it made it possible to rely on accurate ab initio calculations. Moreover, since MOF-74 is an LTE material,[41,57] the assumption of a negligible temperature dependence of S_{ijkl} appeared well justified.

One of the distinct advantages of the Grüneisen theory of thermal expansion is its ability to provide information on the contributions of specific phonon modes, λ, to the thermal expansion tensor. These mode contributions, α_{ij}^{λ}, can be defined in a straightforward manner by combining the thermal averaging of the Grüneisen tensor in Equation (2) with the general expression for α in Equation (3). This yields Equations (4) and (5), which define the mode contributions to α_{ij}. They depend on the compliance tensor, the mode Grüneisen tensor, γ_{ij}^{λ}, and the mode contribution to the phonon heat capacity, $c_v{}^{\lambda}$ (with N_q being the number of wave vectors used to sample reciprocal space):

$$\alpha_{ij}(T) = \frac{1}{N_q} \sum_{\lambda} \alpha_{ij}^{\lambda}(T) \tag{4}$$

with

$$\alpha_{ij}^{\lambda}(T) = \frac{1}{V} \sum_{kl} S_{ijkl} c_v^{\lambda}(T) \gamma_{kl}^{\lambda} \tag{5}$$

Due to the symmetry of MOF-74, which belongs to the rhombohedral crystal class, the equations above can be further simplified, as the associated mean Grüneisen tensor (with Cartesian components ij) has only two independent, non-zero elements, $\langle\gamma_{11}\rangle$ and $\langle\gamma_{33}\rangle$ with $\langle\gamma_{11}\rangle = \langle\gamma_{22}\rangle \neq \langle\gamma_{33}\rangle$ and $\langle\gamma_{ij}\rangle = 0$ for $i \neq j$[129] (see also Section S3, Supporting Information). The same applies to the thermal expansion tensor, α_{ij}, with $\alpha_{11} = \alpha_{22} \neq \alpha_{33}$ and $\alpha_{ij} = 0$ for $i \neq j$. Moreover, when again exploiting the symmetries of MOF-74 and rewriting the elements of the compliance tensor in Voigt notation (as detailed for MOF-74, e.g., in ref. [84]), Equation (3) can be simplified to

$$\alpha_{11} = \frac{C_V}{V} \left(\left(S_{11} + S_{12} \right) \langle\gamma_{11}\rangle + S_{13} \langle\gamma_{33}\rangle \right) \tag{6}$$

and

$$\alpha_{33} = \frac{C_V}{V} \left(2S_{13} \langle\gamma_{11}\rangle + S_{33} \langle\gamma_{33}\rangle \right) \tag{7}$$

Given the diagonal form of α, the α_{11} element is equivalent to the thermal expansion coefficient of lattice parameter a (i.e., the lattice parameter perpendicular to the pore of MOF-74), while α_{33} corresponded to that of lattice parameter c (i.e., the lattice parameter in pore direction). The mode contributions, α_{11}^{λ} and α_{33}^{λ}, were defined in analogy to Equation (5) using the same symmetry-inequivalent elements as in Equations (6) and (7).

3. Results and Discussion

3.1. Experimental Results

While MOFs often show notable (negative) thermal expansion coefficients (see Figure 1) and comparably large shifts in the associated XRD peaks, for MOF-74 the peak positions display exceptionally small temperature-induced shifts, as illustrated in **Figure 3**a. This severely complicates the determination of experimental thermal expansion coefficients, especially in view of the rather broad peaks compared, for example, to metals.

Therefore, we evaluated the data using the Bayesian approach described in detail in Section S2, Supporting Information. This yielded the posterior probability distribution functions for the independent lattice constants, a and c (see Figure 3b,c) and for the associated thermal expansion coefficients, α_{11} and α_{33}, shown in Figure 3d,e. Equivalent plots for the temperature dependences of the probability densities of the unit-cell volume, V, and the associated volumetric thermal expansion coefficient, α_V, can be found in Section S2, Supporting Information. Although the probabilistic uncertainty for the thermal expansion tensor elements is relatively large compared to the calculated expectation values, still certain trends can be observed: first and foremost, all data clearly show that the thermal expansion coefficients of MOF-74 are very small, confirming the notion that MOF-74 is an LTE material, as indicated already in the Section 1 (see Figure 1). Moreover, α_{11} tends to adopt slightly negative values, which is consistent with a weak drop of the lattice parameter a in Figure 3b. The situation is more involved for lattice parameter c (see Figure 3c): it appears to grow between 123 K and 298 K and above ≈400 K; correspondingly, α_{33} is positive for a significant fraction of the covered temperature region. There is, however, also a drop between 298 K and ≈400 K, which is accompanied by particularly broad probability distributions at 273 K and at 298 K. The reason for that is not fully understood, but it might be an indication for certain structural rearrangements within the MOF resulting in an increased degree of disorder at those temperatures.

Overall, the data suggest that α_{11} and α_{33} are not only different in magnitude, but also in sign. This interpretation is supported by qualitatively analogous results for magnesium-based MOF-74 measured by means of neutron powder diffraction.[41] We hypothesize that this difference in sign is a consequence of the 1D nature of the pores (channels). As a result of the different signs of α_{11} and α_{33}, the volumetric thermal expansion coefficient, $\alpha_V \approx 2\alpha_{11} + \alpha_{33}$ (see Section S3, Supporting Information), is approximately zero, albeit at an increased level of uncertainty compared to α_{11} and α_{33}.

In passing we note that the temperature plotted on the horizontal axes in Figure 3b–e is the setpoint temperature measured at the temperature sensor inside the sample holder. In spite of the long equilibration times after reaching the setpoint temperature (see Section 2), there is a possibility that this temperature differs notably from the actual sample temperature due to the lack of convective heat transport for the measurements performed in vacuum (see activation of the MOF in the Section 2). Therefore, we additionally considered an uncertainty in the temperature in our Bayesian analysis (by means of Gaussian probability densities with a standard deviation of 20 K centered at the setpoint temperatures) and calculated an average linear expansion coefficient

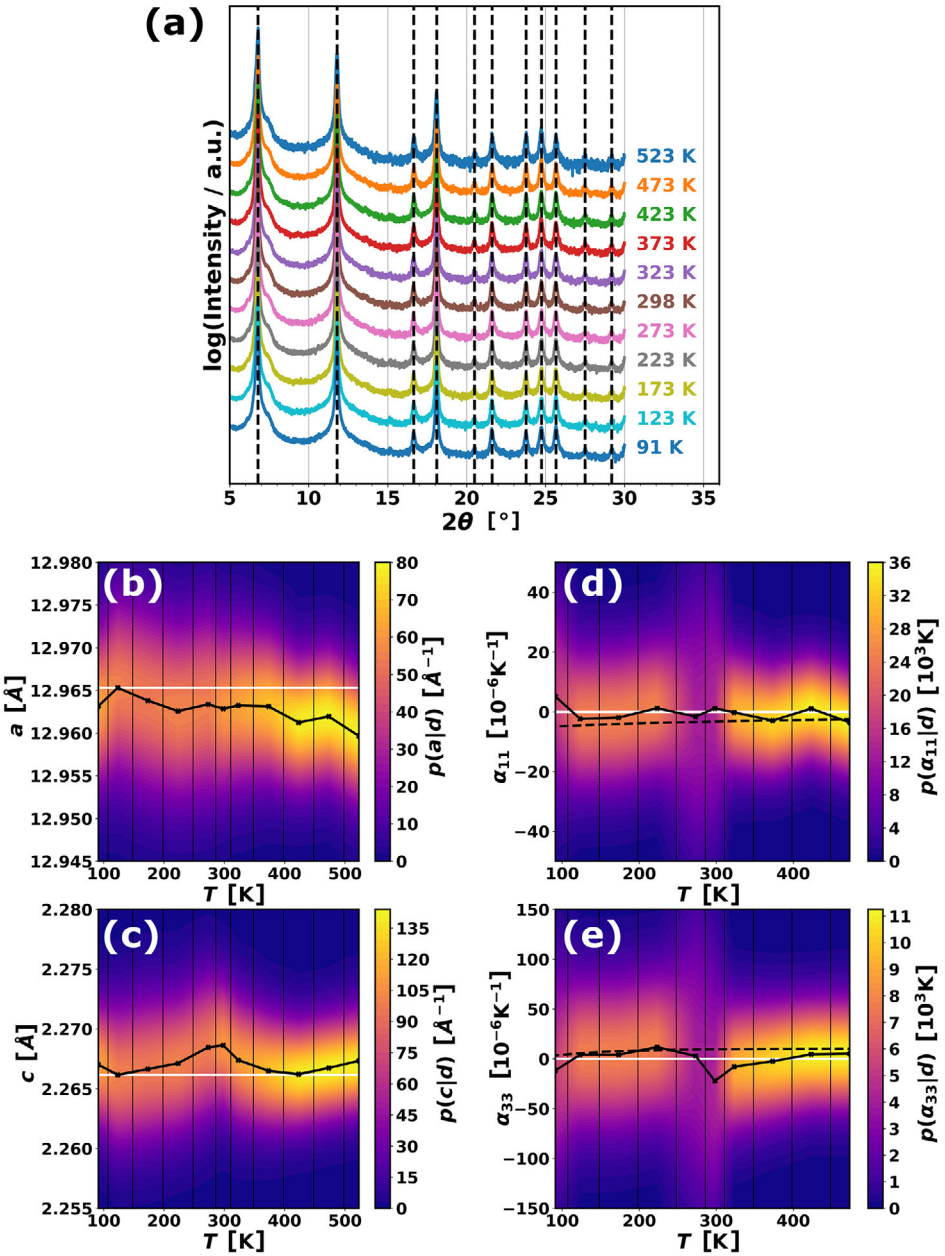

Figure 3. a) Powder XRD patterns of the activated MOF-74 sample for various temperatures. The vertical black dashed lines highlight the (fitted) peak positions at 300 K and serve as guide to the eye, emphasizing the particularly small peak shifts with temperature. b,c) Posterior probability distributions, $p(a|d)$ and $p(c|d)$, (i.e., conditional probability densities given the entirety of experimental data referred to as "d") for the two independent lattice parameters, a and c, as a function of the setpoint temperature obtained from a Bayesian evaluation of the XRD patterns. The white horizontal lines denote the maximum measured value for a and the minimum measured value for c (in terms of their expectation values) for the given temperature range and are guides to the eye. The thin black vertical lines indicate the boundaries of the discrete temperature stripes of which the probability density map is composed. Due to an offset in the lattice parameters between the values obtained from the DFT optimization (at 0 K) and the measured lattice parameters at the lowest temperature (91 K), which is larger than the temperature-induced changes (the simulations underestimate the unit-cell volume by ca. 2%), the theoretical values of $a(T)$ and $c(T)$ are not shown. d,e) Posterior probability distributions, $p(\alpha_{ij}|d)$, for the two independent elements of the thermal expansion tensor, α_{11} and α_{33}, as a function of temperature obtained from a Bayesian evaluation of the XRD patterns. These elements describe the temperature dependence of the lattice parameters a and c, respectively. The thick black lines connect the expectation values of the distributions at each temperature, while the dashed black lines show the temperature dependence of the theoretical results derived from the simulations presented in this work. The white horizontal lines denote the value zero and are guides to the eye. The thin black vertical lines indicate the boundaries of the discrete temperature stripes of which the probability density map is composed.

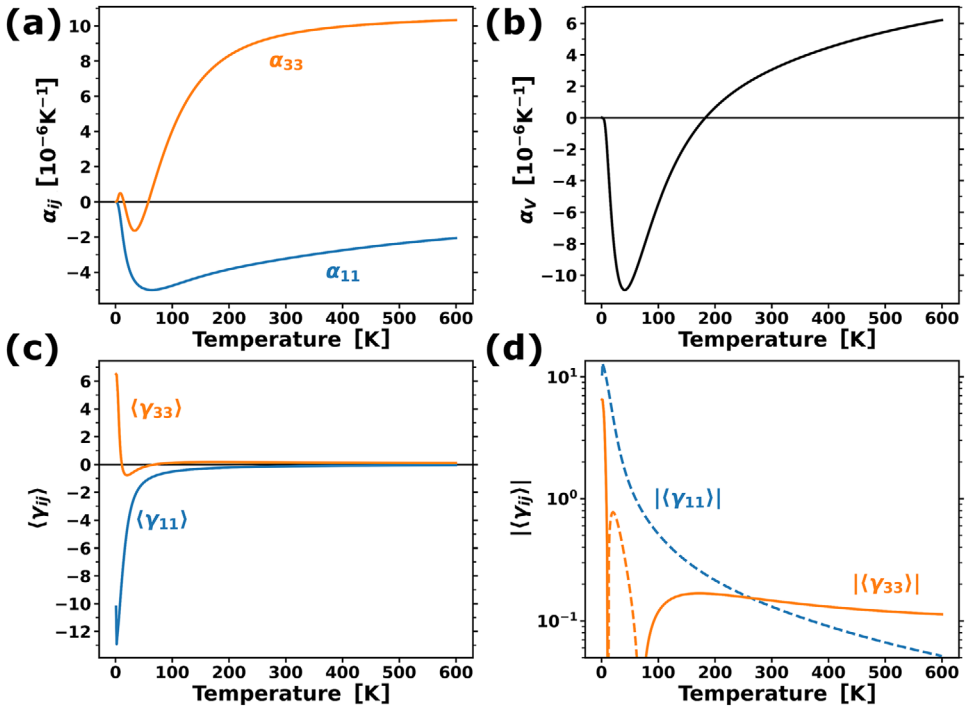

Figure 4. Temperature dependence of a) the two independent components of the thermal expansion tensor, α_{ij}, calculated applying Grüneisen theory, b) the resulting volumetric thermal expansion coefficient, $\alpha_V \approx 2\alpha_{11} + \alpha_{33}$, and c) the two independent components of the mean Grüneisen tensor, $\langle\gamma_{ij}\rangle$, entering the expressions for the thermal expansion tensor. Panel d) contains the absolute value of the two curves shown in panel (c) plotted on a logarithmic scale. Dashed (solid) segments of the lines denote regions in which the mean Grüneisen tensor elements are negative (positive).

for the entire temperature range, $\bar{\alpha}$. This analysis, which is detailed in Section S2.1, Supporting Information, yielded qualitatively unchanged trends of the linear ($\overline{\alpha_{11}} = (-2 \pm 1) \times 10^{-6}$ K^{-1} and $\overline{\alpha_{33}} = (4 \pm 2) \times 10^{-6}$ K^{-1}) and volumetric ($\overline{\alpha_V} = (-1 \pm 4) \times 10^{-6}$ K^{-1}) thermal expansion coefficients.

To unravel the origin of the extraordinarily small (anisotropic) thermal expansion coefficients, we next discuss the results of the ab initio simulations, including a phonon mode-resolved analysis of the relevant contributions to the thermal expansion tensor.

3.2. Theoretical Considerations

3.2.1. Güneisen Theory and Macroscopic Effects

The temperature dependence of the calculated thermal expansion tensor components is plotted in **Figure 4**a, showing NTE perpendicular to the pore ($\alpha_{11} \leq 0$ for all temperatures) and for most temperatures PTE parallel to the pore ($\alpha_{33} > 0$ for temperatures > 70 K). The volumetric thermal expansion coefficient is given by $\alpha_V \approx \mathrm{tr}(\alpha_{ij}) = 2\alpha_{11} + \alpha_{33}$. Due to the simultaneous NTE and PTE behavior of the material around room temperature the calculated value of α_V becomes extremely low ($\approx 3 \times 10^{-6}$ K^{-1} at 300 K), as shown in Figure 4b. This is consistent with the experimental finding.

Beyond the partial cancellation of α_{11} and α_{33} for α_V, also the individual tensor components are relatively small ($|\alpha_{11}| < 5 \times 10^{-6}$ K^{-1} and $|\alpha_{33}| < 10.3 \times 10^{-6}$ K^{-1}), especially in view of the large (negative) thermal expansion coefficients frequently observed in MOFs and other porous materials (see Figure 1). This suggests that also for the individual tensor elements certain cancellation effects occur, which keep the thermal expansion at such low values.

To identify these cancellation effects, the role of the compliance and the mean Grüneisen tensor in Equations (6) and (7) will be analyzed as a next step (see Section 2). Before discussing the more intricate influence of the mean Grüneisen tensor, it is useful to briefly comment on the role of the compliance tensor elements appearing in Equations (6) and (7). A more in-depth discussion of the elastic properties of MOF-74 can be found in ref. [84], which also includes a discussion of their atomic origins. Here it is necessary to highlight that only four out of the seven[84] independent elements of $\boldsymbol{S}$ play a role for thermal expansion within Grüneisen theory: the two elements S_{11} and S_{33} couple stress and strain that are both oriented in x-(or y-) and z-direction, respectively. The other two elements, S_{12} and S_{13}, couple stress and strain in x- and y-direction (both perpendicular to the pore) with the corresponding quantities in y- (or x-) and in z-direction (i.e., perpendicular and parallel to the pore), respectively.

The compliances with the largest (absolute) magnitude are S_{11} and S_{12} ($S_{11} = 180$ TPa^{-1}, $S_{12} = -155$ TPa^{-1}, obtained employing the PBEsol functional; similar values have been obtained for PBE (see ref. [84]; Section S5, Supporting Information). They, however, appear only as a sum in Equation (6) and, due to their different signs, the sum $S_{11} + S_{12}$ amounts to only 25 TPa^{-1}. This substantial cancellation is a result of the fact that when MOF-74 is exposed to, for example, compressive uniaxial stress in x-direction, the resulting compression in x-direction almost equals

the perpendicular expansion in *y*-direction. Consequently, simultaneous stress in the *x*- and *y*-directions triggers expansions and compressions both in *x* and *y*, which largely cancel each other. In passing we note that this compensation effect not only impacts thermal expansion, but also results in a particularly small compressibility in the *xy*-plane (as discussed in more detail in ref. [84]). Despite the above-described cancelation effect, the first term in Equation (6) still dominates α_{11}, as the compliance S_{13}, which couples stress and strain parallel and perpendicular to the pore axis, is even smaller than $S_{11} + S_{12}$ ($S_{13} = -3$ TPa^{-1}). Overall, as both compliance-related prefactors in Equation (6) are relatively small, it is not surprising that α_{11} also remains relatively small at all temperatures ($|\alpha_{11}| < 5 \times 10^{-6}$ K^{-1}).

Notably, similar cancellation effects do not appear for α_{33}, since S_{33} and S_{13} enter Equation (7) separately. This lack of cancellation in the direction of the pores is again consistent with the mechanical properties of MOF-74, where one finds that the compressibility in *z*-direction is much larger than in the *xy*-plane.[84] The fact that S_{33} (=68 TPa^{-1}) is more than 11 times larger than $|2S_{13}|$ (=−6 TPa^{-1}), suggests that the $\langle\gamma_{33}\rangle$-related term in Equation (7) should dominate the evolution of α_{33}.

Nevertheless, a complete picture concerning the sign and the magnitude of the thermal expansion tensor elements can only be obtained when also considering the temperature dependence of the two independent elements of the mean Grüneisen tensor, $\langle\gamma_{ij}\rangle$, which are plotted in Figure 4c. Their absolute values are plotted also in Figure 4d on a logarithmic scale.

Notably, for temperatures above 100 K, both $|\langle\gamma_{11}\rangle|$ and $\langle\gamma_{33}\rangle$ are very small (below 0.51 and 0.19, respectively). The different signs of the components of the mean Grüneisen tensor in combination with the signs of the relevant compliance tensor elements discussed above lead to small negative values of α_{11} and small positive values of α_{33}, consistent with the trends of weak negative and positive thermal expansion of the lattice parameters *a* and *c* deduced from the experiments.

For temperatures below 100 K, the components of the mean Grüneisen tensor display a pronounced temperature dependence: $\langle\gamma_{11}\rangle$ keeps its negative sign, but its absolute value increases significantly at low temperatures. As a result, also the dominating term in Equation (6) increases, resulting in a larger negative thermal expansion coefficient α_{11}. The reason for the less pronounced increase of α_{11} compared to $\langle\gamma_{11}\rangle$ at low temperatures is the diminishing heat capacity C_V. The evolution of $\langle\gamma_{33}\rangle$ is fundamentally different: it starts out positive, becomes negative in a narrow temperature window (12 K $\leq T \leq$ 70 K), and finally returns to the positive regime for high temperatures. This evolution is again directly correlated with the temperature dependence of α_{33}, which switches sign in a similar temperature range. The reason for α_{33} still showing comparably high values above 100 K is the increasing heat capacity in combination with $\langle\gamma_{33}\rangle$ dropping only rather weakly at higher temperatures.

We note in passing that the calculated heat capacities at constant pressure (stress) and at constant volume (strain) are essentially the same (see Section S3.1, Supporting Information). As the difference between the heat capacities depends on products of thermal expansion tensor elements, this can be understood from the small thermal expansion coefficients due to the cancellation effects for the compliance tensor elements and the generally relatively small mean Grüneisen tensor elements.

The above considerations show that the thermal expansion behavior, on the one hand, is determined by the material's elastic properties (i.e., its compliance tensor), while, on the other hand, also the mean Grüneisen tensor plays a crucial role. As mentioned above, a microscopic explanation for the elastic properties of MOF-74(Zn) based on stress-induced atomistic displacements is already contained in ref. [84]. A detailed explanation for the characteristics of the Grüneisen tensor has, however, not been provided yet. It requires an understanding of how its components depend on the individual phonon modes of the material. This understanding will be provided in the following section.

3.2.2. Microscopic Origin: Phonon-Resolved Properties

The phonon-resolved contributions to the thermal expansion, α_{ij}^{λ}, and the mode Grüneisen tensor components are shown in **Figure 5**a–d. Note that, in order to account for the rapid decrease of the γ_{ij}^{λ} and α_{ij}^{λ} with phonon frequency, the frequency scale is plotted logarithmically (equivalent plots with linear frequency scales can be found in Section S8, Supporting Information). Figure 5a,b shows that the mode Grüneisen tensor elements become very small above ≈10 THz, and the most relevant modes are found below ≈3 THz. When considering their contributions to the thermal expansion tensor, α_{ij}^{λ}, the mode contribution to the heat capacity, ${c_v}^{\lambda}$, acts as another low-pass filter. Therefore, α_{ij}^{λ} (in contrast to γ_{ij}^{λ}) is temperature-dependent. Consequently, for low temperatures the frequency up to which phonon modes contribute to the thermal expansion is further reduced. This is explicitly shown for 10 K by the light blue and yellow data points in Figure 5c,d.

Conversely, for temperatures >300 K, the mode Grüneisen tensor elements show a similar frequency dependence as the α_{ij}^{λ}; that is, at room temperature ${c_v}^{\lambda}$ only excludes modes which do not show relevant mode Grüneisen tensor elements. As a consequence, at even higher temperatures, the values of α_{ij}^{λ} hardly change anymore. This is shown in Figure 5c,d for a temperature of 500 K (dark blue and dark red data points).

To avoid the false impression that a significant portion of the overall phonon spectrum contributes significantly to thermal expansion, Figure 5e,f compares the density of phonon states (DOS) per logarithmic frequency interval, DOS_{φ} (for mathematical details see Section S6, Supporting Information) plotted on a logarithmic frequency scale (analogous to panels (a–d)) with a conventional density of states plotted over a linear frequency scale. The vertical dashed lines in both plots refer to the frequency of 3 THz above which the components of the mode Grüneisen tensor become very small. This clearly illustrates that the modes with appreciable values of γ_{ij}^{λ} and, thus, α_{ij}^{λ} cover only a small fraction of the entire phonon spectrum of MOF-74.

The observation that most phonon states are at higher frequencies, where the mode Grüneisen tensor elements have small values, directly impacts the temperature dependence of the mean Grüneisen tensor elements: when the temperature rises, an increasing portion of the modes with particularly small γ_{ij}^{λ} values becomes occupied, such that the averaging process described in Equation (2) generates very small values of $\langle\gamma_{ij}\rangle$ as shown in Figure 4c,d. This is another key reason for the particularly small thermal expansion coefficients of MOF-74 at room temperature.

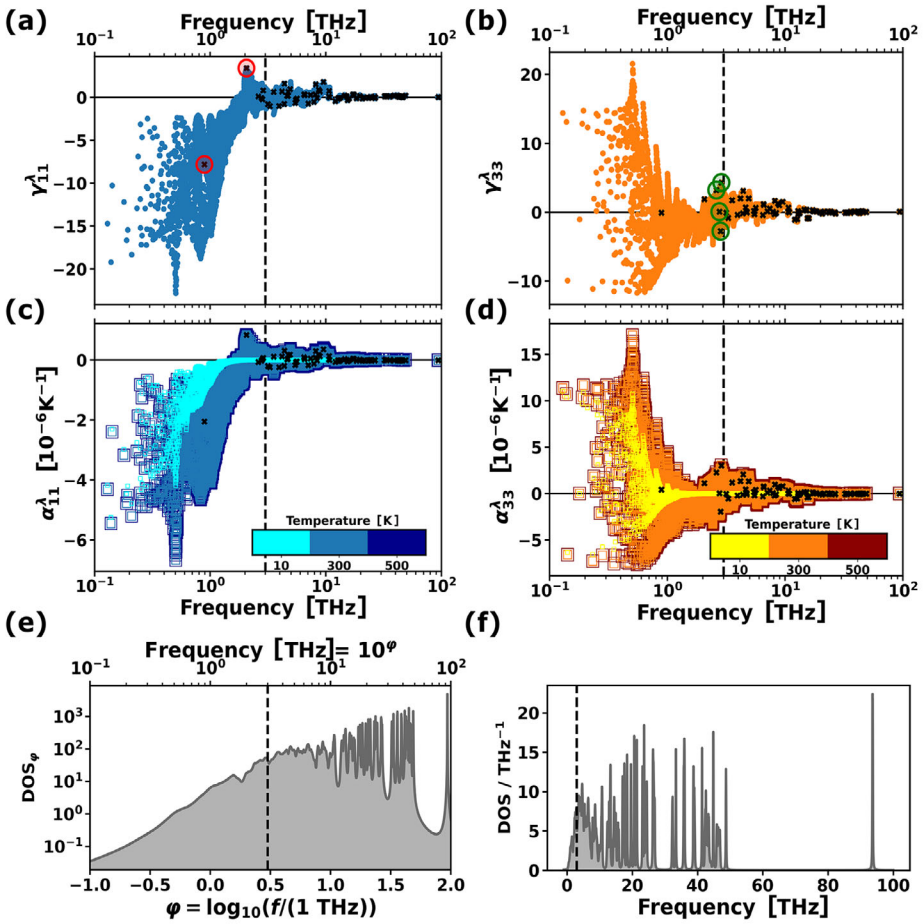

Figure 5. a,b) 11- and 33-components of the mode Grüneisen tensor and c,d) mode contributions to the 11- and 33-components of the thermal expansion tensor at 10, 300, and 500 K of MOF-74 as a function of the phonon frequency. The colored data points correspond to the values for modes sampling the entire first Brillouin zone on a 20 × 20 × 20 mesh of wave vectors. In contrast, the black crosses denote the values for phonons at the Γ-point. The Γ-modes highlighted by semi-transparent circles in panels (a) and (b) are the optical modes, whose displacement patterns are displayed in **Figure 6** and **Figure 7**, respectively. The symbols in panels (c) and (d) are plotted with increasing size for higher temperatures to facilitate the visual recognition. Panel e) shows the density of states per logarithmic frequency interval, DOS$_{\varphi}$, plotted on a logarithmic frequency scale, while panel f) displays the conventional density of states (DOS) and features a linear frequency scale. The detailed differences between the two quantities are explained in Section S6, Supporting Information. The vertical dashed lines in all panels are drawn at a frequency of 3 THz and serve as guide to the eye.

Considering that the mode dependences of α^{λ}_{ij} and γ^{λ}_{ij} are essentially identical for temperatures >200 K, the following more in-depth discussion will be based on the data for γ^{λ}_{11} and γ^{λ}_{33} shown in Figure 5a,b. They contain the following key messages: i) the 11-components of the mode Grüneisen tensors are primarily negative (i.e., compressive strain in *x*- or *y*- direction decreases the frequency of those phonons, which is referred to as "phonon softening") ii) conversely, the 33-components show negative and positive contributions, with a dominance of the latter (i.e., compressive strain in *z*-direction primarily increases the frequency of the phonons). iii) The magnitudes of the 11-components are typically somewhat larger than those of the 33-components (note the different scales in the figures). iv) Finally, the contributions of the Γ-phonons (denoted as the black crosses in Figure 5a–d) typically deviate from those due to phonons with non-vanishing wave vector (especially ≤ ca. 2 THz). This emphasizes that calculations of α_{ij} based only on the (more easily accessible) Γ-phonons are prone to missing the key anharmonicities responsible for the thermal expansion. In the following sections, we will separately discuss the most relevant optical and acoustic modes.

3.2.3. Role of the Optical Phonons

Despite the fact that also off-Γ phonons play a crucial role, for assessing the nature of the most relevant optical phonon bands with large mode Grüneisen parameters, it is useful to analyze the corresponding eigenmode displacements at the Γ-point. This is because—in the absence of avoided crossings—bands typically keep their qualitative character. Moreover, the Grüneisen tensor elements for the optical modes do not change as significantly throughout reciprocal space as those of the acoustic modes. For the analyzed optical Γ-modes, which are highlighted by semi-transparent circles in Figure 5a,b, the mode Grüneisen parameters are typically larger than those of higher-lying Γ-phonons. In

the following discussion, it also must be kept in mind that, overall, the mode Grüneisen parameters at Γ in MOF-74 are smaller in comparison to those in other MOFs,[52,55,67,130] since one is dealing with an LTE material. Thus, the encountered correlations are expected to be sometimes less obvious than for a material with large positive or negative thermal expansion coefficients.

The relevant optical modes either typically involve pronounced motions of the metal nodes relative to the docking groups of the linkers, or they correspond to modes in which the linkers move approximately as rigid units ("rigid unit modes"[131–135]). The latter have actually been associated with negative thermal expansion effects observed in other MOFs.[34,54,56] Considering the nature of these modes, it is useful to not only follow the displacement patterns per se. Additionally, one ought to account for the evolutions of the descriptors defined in Section 2 (Figure 2c,d) in case of i) applied strains and for ii) the motion induced by specific modes. Within the harmonic approximation, the displacements of individual atoms show a strictly sinusoidal time dependence. This is, however, typically not the case for the more complex descriptors. Consequently, the excitation of specific phonons will induce net positive or net negative changes of the time averages of the descriptors relative to their equilibrium values (for more details see Section S10, Supporting Information).

The first two optical modes at 0.89 THz ($\gamma_{11}^{\lambda} \approx -7.80$) and 2.05 THz ($\gamma_{11}^{\lambda} \approx +3.45$) show comparably large values of $|\gamma_{11}^{\lambda}|$. They primarily correspond to rotations of the nodes around their axes (see **Figure 6**a,b and animations, Supporting Information). The higher-frequency mode (Figure 6b) is characterized by rotations of all nodes in the same direction, while they rotate in alternating directions for the lower mode (Figure 6a). Although both modes display a relatively large level of anharmonicity (i.e., large Grüneisen tensor elements), only the lower one shows "phonon softening," as its frequency decreases upon compression in *x*-(or *y*-)direction; that is, the associated 11-element of the mode Grüneisen tensor has a negative sign.

The different signs of the 11 mode component of the Grüneisen parameters of these modes can be understood from comparing the atomic motions in Figure 6a,b and by computing the evolutions of the geometric descriptors of MOF-74 as a function of the displacements along the normal mode coordinates. In the lower frequency mode, as a result of the alternating node rotation, the linkers periodically move inward and outward relative to the pore center, similar to a bending motion. This mode is very similar to the "trampoline mode" partly responsible for the negative thermal expansion in MOF-5[29,31,32,52,55] and HKUST-1.[34] The inward- and outward motion of the linkers result in an increase of their average lengths, which is energetically unfavorable due to their stiffness.[84] The average cross-sectional area of the nodes also increases, and, ideally, the diameter of the pores would decrease such that there is less need for linker stretching. However, a change in the unit-cell parameters is conceptually impossible for Γ-point modes and is, therefore, not visible in Figure 6a. It is nevertheless implied that, due to the anharmonicity of the actual potential, exciting the mode at 0.89 THz favors pore shrinking and, thus negative thermal expansion. In other words, if compressive *x*-stress were applied to the MOF, the motion associated with this phonon mode would be easier to accomplish, which would reduce the stiffness of the mode and, hence, its frequency such that the associated Grüneisen tensor element is negative.

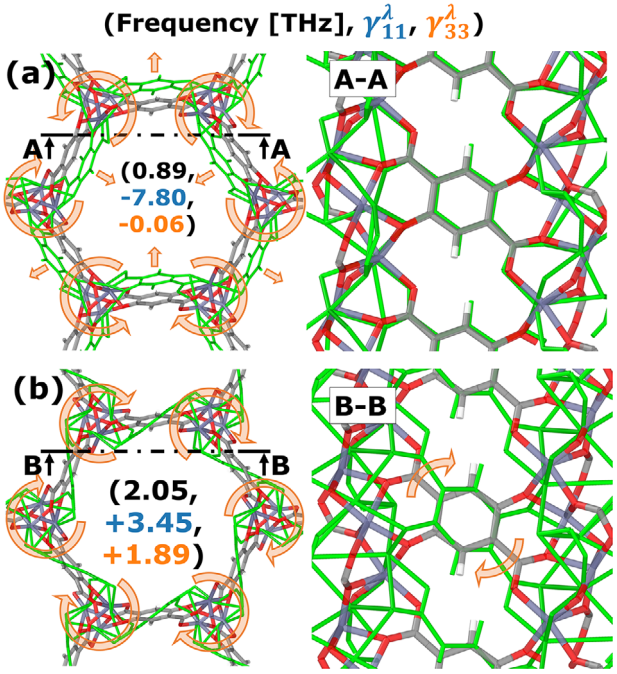

Figure 6. Displacement patterns of the two lowest optical modes with large $|\gamma_{11}^{\lambda}|$-values for MOF-74 plotted for the Γ-point phonons. Panel a) shows the situation for band 4 (at 0.89 THz) and panel b) for band 5 (at 2.05 THz). The Γ-frequency (black text color) as well as the 11- and 33-components of the associated Grüneisen tensors (blue and orange text color) are shown for each mode in parentheses. The undisplaced geometry is shown in element-specific colors representing the respective atoms (C: gray, H: white, O: red, and Zn: purple), while the structures displaced along the eigenmodes are shown in green. The relevant motions are stressed by arrows. The right panels show the cross sections indicated by the black dash-dotted lines in the left columns (i.e., they illustrate the motions in the pore walls).

In contrast, the frequency of the second mode involving linker rotations (shown in Figure 6b) increases upon compressive *x*-(or *y*-)strain. The most prominent change of an average geometric descriptor for this mode is a decrease in the linker inclination, ϕ. This parameter decreases also when applying compressive strain in the *xy*-plane (see Section S10, Supporting Information). An observation that we consistently make is that, when dominant parameters change in the same direction due to compressive strain and the excitation of the respective phonon, the corresponding mode Grüneisen parameter is positive (see also below). We attribute that to the fact that in such a case a simultaneous compression of the MOF and an excitation of the phonon displace the system more significantly from the global equilibrium position. Due to the nature of the anharmonicities, this leads to an increase of the phonon frequency.

Interestingly, "inclination modes" of the linker moieties similar to the mode at 2.05 THz were found in MOF-5 to contribute to the opposite effect, namely to negative thermal expansion.[29,31,32,52,55] This can be understood from the fact that in MOF-5 one starts from perfectly straight linkers such that an "inclination mode" increases the average linker inclination and shortens the unit cell, in contrast to the effect found in MOF-74.

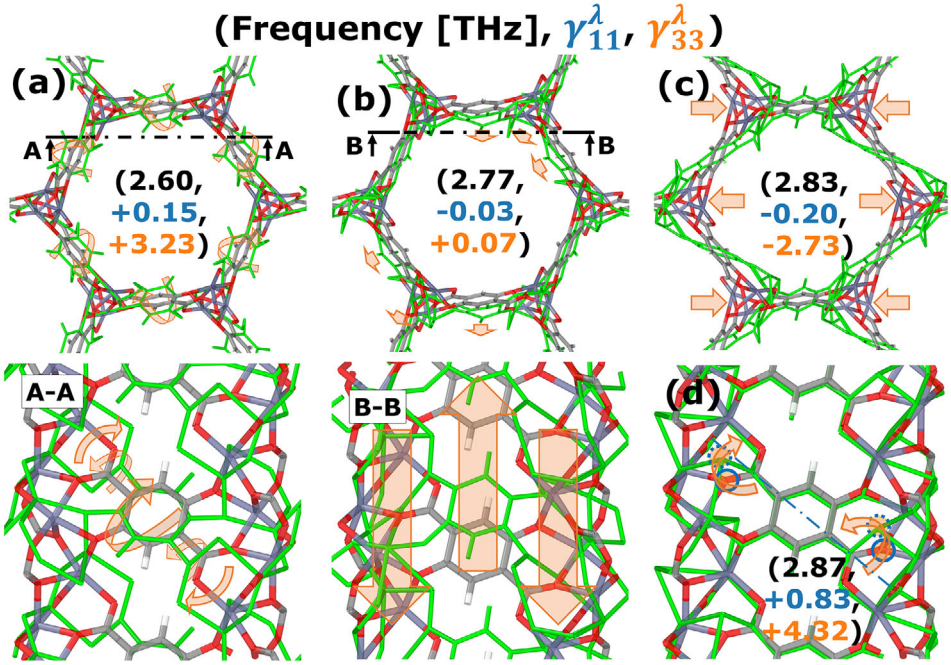

Figure 7. Displacement patterns of low-frequency optical phonon modes with large (or particularly small) $|\gamma_{33}^{\lambda}|$-values for MOF-74 plotted for the Γ-point phonons. Panel a) shows the situation for band 6 (at 2.60 THz), panel b) for band 8 (at 2.77 THz), panel c) for band 9 (at 2.83 THz), and panel d) for band 11 (at 2.87 THz). Except for the mode in panel (b), all displayed modes show comparably large values of $|\gamma_{33}^{\lambda}|$. The Γ-frequency (black text color) as well as the 11- and 33-components of the associated Grüneisen tensors (blue and orange text color) are shown for each mode in parentheses. The undisplaced geometry is shown in element-specific colors representing the respective atoms (C: gray, H: white, O: red, and Zn: purple), while the structures displaced along the eigenmodes are shown in green. The relevant motions are stressed by arrows. The bottom panels of panels (a) and (b) show cross sections indicated by the black dash-dotted lines in the top panels (i.e., they illustrate the motions in the pore walls). Notably, there are two pairs of bands, which are degenerate at the Γ-point at 2.77 and at 2.83 THz (bands 7 and 8 as well as bands 9 and 10). Of those, only the Γ-phonons of band 8 and 9 are shown in panels (b) and (c). The other ones involve similar atomic motions (see animations in the Supporting Information). The blue circles in panel (d) highlight the (carboxylic) oxygen atom which exhibits the most notable torsional motion.

As the strain-dependence of the above-discussed modes is intimately connected to the pore diameter rather than to the lattice parameter c (along the nodes), the frequencies of the modes change only very little for strain in z-direction, which results in small associated Grüneisen tensor elements, γ_{33}^{λ}. Conversely, most of the remaining optical modes below 3 THz exhibit a more pronounced anharmonic character for z-strain. The mode at 2.60 THz displayed in **Figure 7**a shows a comparably large positive γ_{33}^{λ} element (+3.23). The associated atomic motion again involves a variation in the linker inclination, ϕ, and also in the linker tilt, θ, albeit here the average angles increase. Additionally, one can observe an increase in the average node cross-sectional area, A_{Δ}, which impacts the local Zn–O bonding geometry of the nodes such that the average dihedral angle, τ, between the COO^{-} group and the aromatic ring decreases. Upon compression in z-direction, both A_{Δ} and τ increase considerably. Considering the flat torsional potential of the COO^{-} group (as shown for IRMOFs[67]), the increase of A_{Δ} apparently dominates such that, in line with the above arguments, γ_{33}^{λ} is positive.

The next higher optical, twofold degenerate mode at 2.77 THz shows comparably small Grüneisen tensor elements, both, for the 11- and the 33-component (see Figure 7b). This might be because they primarily trigger a deformation of the hexagonal shape of the pore, which is a very soft degree of freedom in MOF-74.[84] In z-direction, the MOF experiences no drastic structural changes for this vibration: the nodes and linkers are shifted alternatingly in $+z$ and $-z$ direction, which is not a deformation observed when applying z-strain.

The last two modes discussed here are again more relevant for the thermal expansion of MOF-74: the twofold degenerate mode at 2.83 THz characterized by deformations of the pore shape (see Figure 7c) and the mode at 2.87 THz characterized by torsion of the COO^{-} groups of the linkers (see Figure 7d). They display negative (−2.73) and positive (+4.32) values of γ_{33}^{λ}, respectively. For the 2.83 THz mode with negative Grüneisen tensor elements, one can rationalize the strain-induced phonon softening considering that z-compression and the phonon mode act in opposite directions: during the (comparably soft) pore-deformation the average node area, A_{Δ}, decreases and the linkers become flatter, that is, θ increases. The opposite applies to the 2.87 THz mode: here, the most relevant vibration-induced changes in the average geometric descriptors are increases of τ and A_{Δ}, which are both also triggered by compressive z-strain.

3.2.4. Role of the Acoustic Phonons

Despite the impact of the optical phonons, the largest contributions to the thermal expansion tensor arise from acoustic phonons with finite wave vectors, as previously indicated in

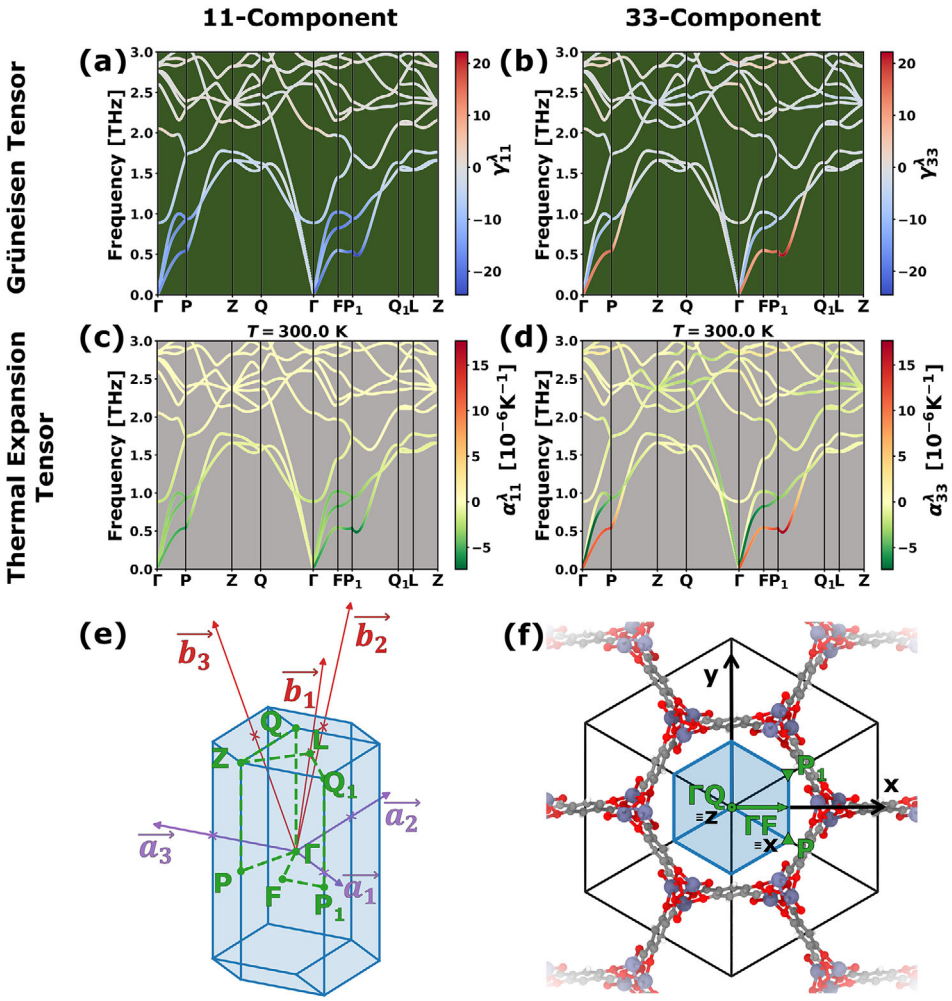

Figure 8. PBEsol/D3-BJ-calculated phonon band structure of MOF-74 colored according to a,b) the mode Grüneisen tensor components, γ_{11}^{λ} and γ_{33}^{λ}, and c,d) the mode contributions to the thermal expansion tensor components, α_{11}^{λ} and α_{33}^{λ}, (see Equation (5)). e) First Brillouin zone of MOF-74 including the lattice parameters, $\vec{a_n}$, the reciprocal lattice vectors, $\vec{b_n}$, and the high-symmetry points between which the band structures are drawn. f) Directions of the high-symmetry paths ΓQ and ΓF in real space. They correspond to the *z*- and the *x*-axis, respectively and are, thus, parallel and perpendicular to the pore direction. The high-symmetry points P and P_1 lie slightly above and below the *xy*-plane and are denoted by an upward and a downward pointing triangle.

Figure 5. The corresponding bands display a particularly large dispersion. Therefore, it is useful to analyze the associated mode Grüneisen constants in a wave-vector resolved fashion. The calculated low-frequency phonon band structure (≤3 THz) for MOF-74 is shown in **Figure 8** with the bands colored according to the elements of the mode Grüneisen tensors (a) and (b) and the respective mode contributions to the thermal expansion tensor (c) and (d). As the trends are similar for both quantities, we will again focus the discussion on the elements of the (mode) Grüneisen tensors.

Figure 8a,b confirms that the largest mode Grüneisen tensor elements are found for the acoustic bands below 1 THz. This is particularly true for phonons propagating in or close to the *xy*-plane of the structure, that is, for bands toward the high-symmetry points F, P, and P_1. Interestingly, the two higher acoustic bands are characterized by negative values for γ_{11}^{λ} and γ_{33}^{λ} in the entire Brillouin zone. Conversely, the lowest acoustic band show negative γ_{11}^{λ} tensor elements, while the γ_{33}^{λ} elements are particularly large and positive. This causes the overall positive sign of γ_{33}^{λ} (for the impact of the chosen functional on this trend mentioned already in Section 2, see Section S5, Supporting Information).

To understand the sign change between γ_{11}^{λ} and γ_{33}^{λ}, it is again useful to consider the mode displacement pattern of the lowest acoustic mode at the high symmetry point F. This displacement pattern is shown in **Figure 9**a (animations can be found in the Supporting Information). It reveals that this acoustic mode has primarily transverse character, with the phonon polarization vectors showing nearly no components in *z*-direction (i.e., along the pores). For waves propagating in *x*-direction (along ΓF), the polarization of the said transverse acoustic phonons is oriented nearly fully in *y*-direction. At the F-point, neighboring nodes move in opposite directions (with correspondingly smaller phase shifts

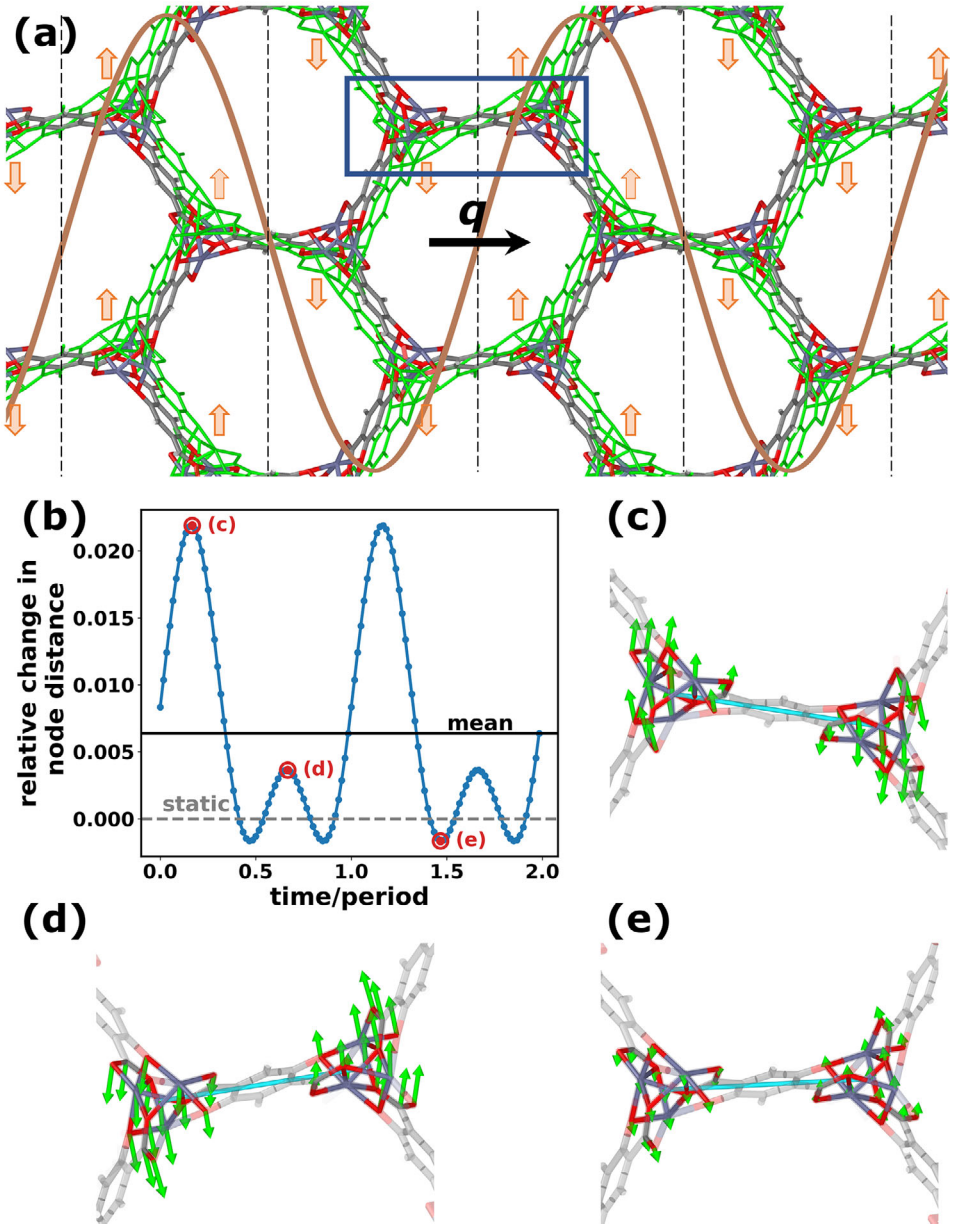

Figure 9. a) Displacement pattern of the lowest transverse acoustic phonon at the F-point (with the reduced wave vector [0.5, −0.5, 0]). The undisplaced geometry is shown in element-specific colors representing the respective atoms (C: gray, H: white, O: red, and Zn: purple), while the structures displaced along the eigenmodes are shown in green. The wave vector is oriented in *x*-direction (see black arrow denoting the wave vector ***q***, while the polarization is primarily oriented in *y*-direction as denoted by the orange arrows as well as the sinus-shaped waves implying the polarization amplitude. The vertical dashed black lines indicate the nodal planes of the standing waves, that is, the planes with vanishing displacements. The dark blue rectangle indicates the zoomed-in region shown in panels (c–e). b) Time evolution of the change in distance between the axes of two neighboring nodes (i.e., the length of the blue line in panels (c–e)) during the atomic motion associated with the transverse acoustic phonon at F relative to the static (0-K optimized) value. The mean value of the node distance is drawn as a black horizontal line, while the static value is denoted by a grey dashed line. The snapshots of the motion in panels (c–e), in which the node distance is shown as a light blue line, are indicated by red circles in panel (b).

for smaller ***q***). As a consequence, the average distance between the nodes increases, as shown in Figure 9b (selected snapshots of the motion associated with this acoustic phonon at F are shown in Figure 9c–e). This again results in the energetically very costly stretching of the linker molecules, which can be compensated by a unit-cell shrinkage, when this mode is increasingly excited with temperature. This causes a phonon softening and, thus, contributes to the negative thermal expansion in the *xy*-plane. Overall, this situation is reminiscent of similar observations reported for MOF-5.[52] Conversely, when MOF-74 is strained in *z*-direction, the nodes expand, but they also rotate such that the linkers are slightly elongated. The tendency to increase the linker length for *z*-strain and for the phonon displacement is again held responsible for the positive sign of the corresponding

mode-Grüneisen tensor parameter γ^{λ}_{33}. This mode is additionally accompanied by a net lateral expansion of the nodes (an increase in A_{Δ}) and a rotation of the nodes, η, like for compressive strain in z-direction.

Similar transverse acoustic modes with a "dual" character, that is, a positive value of γ^{λ}_{33} and a negative value of γ^{λ}_{11} are observed, for example, for the ΓP and FP_1 directions (i.e., for wave vectors almost perpendicular to the pore). Interestingly, such modes do not occur for wave vectors parallel to the pore and here in particular in the ΓQ-direction. We attribute this to the observation that no modes with a strictly transverse character with displacements in the xy-plane occur for the respective $\boldsymbol{q}$-direction, which results in only comparably small mode Grüneisen parameter components.

3.2.5. Understanding the Impact of the Used Functional

Based on the above considerations it shall be briefly explained, why the PBE functional erroneously (as argued in the Section 2) yields a negative thermal expansion along the pore of MOF-74. A more detailed discussion can be found in Sections S4, S5, Supporting Information: upon compressing the unit cell along the pore, the linker is elongated when using the PBEsol functional, while it is compressed with PBE (see Section S5.3, Supporting Information). At the same time, the phonon-induced changes in the geometric descriptors obtained with both functionals are very similar: the transverse acoustic modes in directions (close to) perpendicular to the pore, on average, cause an increase of the linker length. Consistent with the above discussion, the fact that in PBEsol calculations strain and phonons qualitatively affect the linker length in the same way favors positive Grüneisen tensor 33-elements. Conversely, with PBE strain and phonons result in opposite changes of the (average) linker length, which explains the negative 33-component of the Grüneisen tensor for transverse acoustic modes in directions (close to) perpendicular to the pore. Interestingly, we find positive thermal expansion along the pore also with PBE when considering (unrealistically) larger strain magnitudes, as extensively tested in various QHA-based approaches (see Sections S4, S5, Supporting Information). We hypothesize that the inconsistency for small strains is closely related to the quasi-1D nature of the pores. As a consequence, the pore walls extended in z-direction are reminiscent of a densely packed solid, for which the PBEsol functional is supposed to yield more accurate structural properties[90,91,110] and thermal expansion coefficients.[70,111,112] In passing we note that also the lattice parameter c is somewhat larger with PBE than with PBEsol in our unit cell optimizations (by ≈0.8%). This is consistent with the notion that lattice constants tend to be (more significantly) overestimated with PBE compared to PBEsol.[90,91,110] Here, ≈0.8% might appear small, but it is of the same order of magnitude as the expansion of c as a result of a temperature difference of several hundred K.

4. Conclusions

The presented work combines temperature-dependent X-ray diffractometry with state-of-the-art dispersion-corrected DFT simulations (within the Grüneisen theory) to explain the atomistic origin of the low thermal expansion observed for pristine, zinc-based MOF-74. Comparing the thermal expansion coefficients in MOF-74 with the situation in other MOFs reported in literature, MOF-74 can be regarded as a low thermal expansion material. This is consistent with the results of the conducted diffraction experiments, revealing very minor temperature-induced shifts of the positions of the diffraction peaks. Therefore, a probabilistic approach is necessary to determine the two independent lattice constants of MOF-74, a and c (related to the pore diameter and the pore length per unit cell, respectively), and the associated components of the Cartesian thermal expansion tensor, $\alpha_{11}(=\alpha_{22})$ and α_{33}.

The obtained probability densities suggest that lattice parameter a decreases with temperature, while c increases for most of the considered temperature range. The volumetric thermal expansion coefficient is very low ($\approx 3 \times 10^{-6}$ K^{-1}) at 300 K due to the different signs of α_{11} and α_{33}. The experimental results are in good qualitative agreement with theoretical results based on the Grüneisen theory of thermal expansion relying on ab initio data. In this context, it has to be kept in mind that it is virtually impossible to achieve a perfect quantitative agreement between theory and experiment for a quantity that is close to zero due to cancellation effects (see below). This also explains, why all our attempts to describe the situation via a free energy minimization within the QHA suffered from serious shortcomings and why the choice of the functional can have even a qualitative impact on the obtained results.

As indicated in the previous paragraph, also the tensor elements, α_{11} and α_{33}, are subject to cancellation effects: within Grüneisen theory, α_{11} and α_{33} arise from sums and products of elements of the compliance tensor, the heat capacity, and the mean Grüneisen tensors, with the latter incorporating the anharmonicities of all phonon modes in the crystal. For α_{11}, the cancellation effect occurs due to close-to-equal compliance tensor elements with different sign ($S_{11} \approx -S_{12}$) resulting in a small value of $|\alpha_{11}| < 5 \times 10^{-6}$ K^{-1} for all temperatures, regardless of the mean Grüneisen tensor. For the latter, a notable magnitude is observed only at low temperatures. The mean Grüneisen tensor also determines the negative sign of α_{11}. For α_{33}, the cancellation effects occur, when determining the mean Grüneisen tensor from the mode contributions due to a similar amount of negative and positive contributions especially below frequencies of ≈2 THz. Only at higher frequencies, the positive contributions clearly dominate resulting in slightly larger positive values of α_{33} (with $|\alpha_{33}|$ remaining below 10.3×10^{-6} K^{-1}).

Overall, the absolute magnitudes of the mode Grüneisen tensor elements, however, display a pronounced drop with frequency and become negligible for frequencies > 10 THz. Therefore, as the temperature increases, an increasing number of optical phonon modes with particularly small contributions to the thermal expansion become excited such that the mean Grüneisen tensor decreases, and the thermal expansion tensor is kept at a very low level.

Whether specific phonons trigger positive or negative thermal expansion is then analyzed by comparing the evolutions of carefully chosen geometric descriptors as a function of i) the applied strains and ii) normal-mode coordinates of the respective phonons. Interestingly, only few of the relevant contributions

stem from phonons at the center of the first Brillouin zone, Γ. This means that the essence of the anharmonicities in MOF-74 is missed, when relying only on Γ-point phonons during the calculation of the thermal expansion tensor. Overall, we identify several optical phonon branches that have an impact on (negative) thermal expansion. The main contributions in MOF-74, however, arise from acoustic phonons propagating in directions almost perpendicular to the pore. In those directions, the main contributions arise from the lowest transverse acoustic bands, which simultaneously favor a reduction of the pore diameter and an expansion of the pore length.

These results show that the thermal expansion in MOFs can be determined by a subtle interplay of a wide variety of factors, which becomes particularly complex in situations dominated by cancellation effects.

Supporting Information

Supporting Information is available from the Wiley Online Library or from the author.

Acknowledgements

The authors thank Timo Müller, Barbara Puhr, and Andrew Jones from the company Anton Paar who provided the infrastructure and their know-how to conduct the temperature-dependent XRD measurements. The authors are also grateful to Paolo Falcaro for his appreciated input and for providing the resources for the sample preparation. T.K. acknowledges funding as recipient of a DOC Fellowship (25783) of the Austrian Academy of Sciences at the Institute of Solid State Physics and the Institute of Physical and Theoretical Chemistry. The authors also acknowledge the Graz University of Technology for financial support through the Lead Project (LP-03) and the use of HPC resources provided by the ZID. The computational results were in part achieved using the Vienna Scientific Cluster (VSC3).

Conflict of Interest

The authors declare no conflict of interest.

Data Availability Statement

The data that support the findings of this study are openly available in the NOMAD database at [https://doi.org/10.17172/NOMAD/2022.03.07-1].

Keywords

Grüneisen tensors, metal–organic frameworks, MOF-74, phonons, thermal-expansion

Received: January 18, 2022
Revised: March 1, 2022
Published online: April 5, 2022

[1] S. L. James, *Chem. Soc. Rev.* **2003**, *32*, 276.
[2] H. Furukawa, K. E. Cordova, M. O'Keeffe, O. M. Yaghi, *Science* **2013**, *341*, 1230444.
[3] J. L. C. Rowsell, O. M. Yaghi, *Microporous Mesoporous Mater.* **2004**, *73*, 3.
[4] S. Kitagawa, R. Kitaura, S. Noro, *Angew. Chem., Int. Ed. Engl.* **2004**, *43*, 2334.
[5] H. Li, M. Eddaoudi, M. O'Keeffe, O. M. Yaghi, *Nature* **1999**, *402*, 276.
[6] M. Hu, H. Lou, X. Yan, X. Hu, R. Feng, M. Zhou, *Microporous Mesoporous Mater.* **2018**, *271*, 68.
[7] O. K. Farha, I. Eryazici, N. C. Jeong, B. G. Hauser, C. E. Wilmer, A. A. Sarjeant, R. Q. Snurr, S. T. Nguyen, A. Ö. Yazaydın, J. T. Hupp, *J. Am. Chem. Soc.* **2012**, *134*, 15016.
[8] M. Eddaoudi, J. Kim, N. Rosi, D. Vodak, J. Wachter, M. O'Keeffe, O. M. Yaghi, *Science* **2002**, *295*, 469.
[9] L. J. Murray, M. Dinca, J. R. Long, *Chem. Soc. Rev.* **2009**, *38*, 1294.
[10] J. L. C. Rowsell, O. M. Yaghi, *J. Am. Chem. Soc.* **2006**, *128*, 1304.
[11] V. Pascanu, G. González Miera, A. K. Inge, B. Martín-Matute, *J. Am. Chem. Soc.* **2019**, *141*, 7223.
[12] J. Liu, L. Chen, H. Cui, J. Zhang, L. Zhang, C. Y. Su, *Chem. Soc. Rev.* **2014**, *43*, 6011.
[13] L. Zhu, X. Q. Liu, H. L. Jiang, L. B. Sun, *Chem. Rev.* **2017**, *117*, 8129.
[14] E. D. Bloch, W. L. Queen, R. Krishna, J. M. Zadrozny, C. M. Brown, J. R. Long, *Science* **2012**, *335*, 1606.
[15] B. Chen, C. Liang, J. Yang, D. S. Contreras, Y. L. Clancy, E. B. Lobkovsky, O. M. Yaghi, S. Dai, *Angew. Chem., Int. Ed.* **2006**, *45*, 1390.
[16] I. Stassen, N. Burtch, A. Talin, P. Falcaro, M. Allendorf, R. Ameloot, *Chem. Soc. Rev.* **2017**, *46*, 3185.
[17] Y. Cui, B. Li, H. He, W. Zhou, B. Chen, G. Qian, *Acc. Chem. Res.* **2016**, *49*, 483.
[18] K. J. Erickson, F. Léonard, V. Stavila, M. E. Foster, C. D. Spataru, R. E. Jones, B. M. Foley, P. E. Hopkins, M. D. Allendorf, A. A. Talin, *Adv. Mater.* **2015**, *27*, 3453.
[19] N. C. Burtch, J. Heinen, T. D. Bennett, D. Dubbeldam, M. D. Allendorf, *Adv. Mater.* **2018**, *30*, 1704124.
[20] V. Stavila, A. A. Talin, M. D. Allendorf, *Chem. Soc. Rev.* **2014**, *43*, 5994.
[21] D. Dubbeldam, K. S. Walton, D. E. Ellis, R. Q. Snurr, *Angew. Chem., Int. Ed.* **2007**, *46*, 4496.
[22] S. J. Baxter, A. Schneemann, A. D. Ready, P. Wijeratne, A. P. Wilkinson, N. C. Burtch, *J. Am. Chem. Soc.* **2019**, *141*, 12849.
[23] R. N. Jacobs, J. Markunas, J. Pellegrino, L. A. Almeida, M. Groenert, M. Jaime-Vasquez, N. Mahadik, C. Andrews, S. B. Qadri, *J. Cryst. Growth* **2008**, *310*, 2960.
[24] J. M. Baribeau, T. E. Jackman, P. Maigné, D. C. Houghton, M. W. Denhoff, *J. Vac. Sci. Technol., A* **1987**, *5*, 1898.
[25] J.-H. Ryou, W. Lee, in *Nitride Semiconductor Light-Emitting Diodes (LEDs)*, Elsevier, Amsterdam **2018**, p. 43.
[26] J. Wieme, V. Van Speybroeck, *J. Mater. Chem. A* **2021**, *9*, 4898.
[27] P. Falcaro, K. Okada, T. Hara, K. Ikigaki, Y. Tokudome, A. W. Thornton, A. J. Hill, T. Williams, C. Doonan, M. Takahashi, *Nat. Mater.* **2017**, *16*, 342.
[28] K. Ikigaki, K. Okada, Y. Tokudome, T. Toyao, P. Falcaro, C. J. Doonan, M. Takahashi, *Angew. Chem., Int. Ed.* **2019**, *58*, 6886.
[29] W. Zhou, H. Wu, T. Yildirim, J. R. Simpson, A. R. H. Walker, *Phys. Rev. B: Condens. Matter Mater. Phys.* **2008**, *78*, 054114.
[30] N. C. Burtch, S. J. Baxter, J. Heinen, A. Bird, A. Schneemann, D. Dubbeldam, A. Wilkinson, *Adv. Funct. Mater.* **2019**, *1904669*, 1.
[31] N. Lock, Y. Wu, M. Christensen, L. J. Cameron, V. K. Peterson, A. J. Bridgeman, C. J. Kepert, B. B. Iversen, *J. Phys. Chem. C* **2010**, *114*, 16181.
[32] N. Lock, M. Christensen, Y. Wu, V. K. Peterson, M. K. Thomsen, R. O. Piltz, A. J. Ramirez-Cuesta, G. J. McIntyre, K. Norén, R. Kutteh, C. J. Kepert, G. J. Kearley, B. B. Iversen, *J. Chem. Soc. Dalt. Trans.* **2013**, *42*, 1996.

[33] S. Krause, V. Bon, I. Senkovska, U. Stoeck, D. Wallacher, D. M. Többens, S. Zander, R. S. Pillai, G. Maurin, F. X. Coudert, S. Kaskel, *Nature* **2016**, *532*, 348.
[34] Y. Wu, A. Kobayashi, G. J. Halder, V. K. Peterson, K. W. Chapman, N. Lock, P. D. Southon, C. J. Kepert, *Angew. Chem., Int. Ed.* **2008**, *47*, 8929.
[35] C. Schneider, D. Bodesheim, M. G. Ehrenreich, V. Crocella, J. Mink, R. A. Fischer, K. T. Butler, G. Kieslich, *J. Am. Chem. Soc.* **2019**, *141*, 10504.
[36] V. K. Peterson, G. J. Kearley, Y. Wu, A. J. Ramirez-Cuesta, E. Kemner, C. J. Kepert, *Angew. Chem., Int. Ed.* **2010**, *49*, 585.
[37] S. Henke, A. Schneemann, R. A. Fischer, *Adv. Funct. Mater.* **2013**, *23*, 5990.
[38] C. Yang, X. Wang, M. A. Omary, *Angew. Chem., Int. Ed.* **2009**, *48*, 2500.
[39] H.-L. Zhou, R.-B. Lin, C.-T. He, Y.-B. Zhang, N. Feng, Q. Wang, F. Deng, J.-P. Zhang, X.-M. Chen, *Nat. Commun.* **2013**, *4*, 2534.
[40] A. F. Sapnik, H. S. Geddes, E. M. Reynolds, H. H. M. M. Yeung, A. L. Goodwin, *Chem. Commun.* **2018**, *54*, 9651.
[41] W. L. Queen, C. M. Brown, D. K. Britt, P. Zajdel, M. R. Hudson, O. M. Yaghi, *J. Phys. Chem. C* **2011**, *115*, 24915.
[42] P. Lama, R. K. Das, V. J. Smith, L. J. Barbour, *Chem. Commun.* **2014**, *50*, 6464.
[43] A. Kondo, K. Maeda, *J. Solid State Chem.* **2015**, *221*, 126.
[44] L. D. Devries, P. M. Barron, E. P. Hurley, C. Hu, W. Choe, *J. Am. Chem. Soc.* **2011**, *133*, 14848.
[45] C. W. Ashling, G. I. Lampronti, T. J. F. Southern, R. C. Evans, D. Bennett, *ChemRxiv* **2021**.
[46] I. Grobler, V. J. Smith, P. M. Bhatt, S. A. Herbert, L. J. Barbour, *J. Am. Chem. Soc.* **2013**, *135*, 6411.
[47] W. Cai, A. Katrusiak, *Nat. Commun.* **2014**, *5*, 4337.
[48] Y. Wu, V. K. Peterson, E. Luks, T. A. Darwish, C. J. Kepert, *Angew. Chem., Int. Ed.* **2014**, *53*, 5175.
[49] J. M. Ogborn, I. E. Collings, S. A. Moggach, A. L. Thompson, A. L. Goodwin, *Chem. Sci.* **2012**, *3*, 3011.
[50] S. R. Madsen, N. Lock, J. Overgaard, B. B. Iversen, *Acta Crystallogr., Sect. B: Struct. Sci., Cryst. Eng. Mater.* **2014**, *70*, 595.
[51] M. Asgari, I. Kochetygov, H. Abedini, W. L. Queen, *Nano Res.* **2021**, *14*, 404.
[52] L. H. N. N. Rimmer, M. T. Dove, A. L. Goodwin, D. C. Palmer, *Phys. Chem. Chem. Phys.* **2014**, *16*, 21144.
[53] S. S. Han, W. A. G. Iii, *J. Phys. Chem. C* **2007**, *111*, 15185.
[54] S. R. G. G. Balestra, R. Bueno-Perez, S. Hamad, D. Dubbeldam, A. R. Ruiz-Salvador, S. Calero, *Chem. Mater.* **2016**, *28*, 8296.
[55] L. Wang, C. Wang, Y. Sun, K. Shi, S. Deng, H. Lu, *Mater. Chem. Phys.* **2016**, *175*, 138.
[56] J. D. Evans, J. P. Dürholt, S. Kaskel, R. Schmid, *J. Mater. Chem. A* **2019**.
[57] P. Canepa, K. Tan, Y. Du, H. Lu, Y. J. Chabal, T. Thonhauser, *J. Mater. Chem. A* **2015**, *3*, 986.
[58] J. Wieme, S. Vandenbrande, A. Lamaire, V. Kapil, L. Vanduyfhuys, V. Van Speybroeck, *ACS Appl. Mater. Interfaces* **2019**, *11*, 38697.
[59] Y. Sun, H. Sun, *J. Mol. Model.* **2014**, *20*, 2146.
[60] O. Guseva, H. R. Lusti, A. A. Gusev, *Modell. Simul. Mater. Sci. Eng.* **2004**, *12*, 1201.
[61] S. D. R. S. Krishnan, R. Srinivasan, B. R. Pamplin, *Thermal Expansion of Crystals*, Pergamon Press, Oxford **1979**.
[62] A. Lamaire, J. Wieme, S. M. J. J. Rogge, M. Waroquier, V. Van Speybroeck, *J. Chem. Phys.* **2019**, *150*, 094503.
[63] S. Wieser, T. Kamencek, J. P. Dürholt, R. Schmid, N. Bedoya-Martínez, E. Zojer, *Adv. Theory Simul.* **2021**, *4*, 2000211.
[64] X. Wang, R. Guo, D. Xu, J. Chung, M. Kaviany, B. Huang, *J. Phys. Chem. C* **2015**, *119*, 26000.
[65] H. Babaei, C. E. Wilmer, *Phys. Rev. Lett.* **2016**, *116*, 025902.
[66] B. L. Huang, A. J. H. H. McGaughey, M. Kaviany, *Int. J. Heat Mass Transf.* **2007**, *50*, 393.
[67] T. Kamencek, N. Bedoya-Martínez, E. Zojer, *Phys. Rev. Mater.* **2019**, *3*, 116003.
[68] R. A. Cowley, *Acta Crystallogr., Sect. A: Found. Crystallogr.* **1975**, *31*, 527.
[69] J. Fabian, P. B. Allen, *Phys. Rev. Lett.* **1997**, *79*, 1885.
[70] E. T. Ritz, S. J. Li, N. A. Benedek, *J. Appl. Phys.* **2019**, *126*, 171102.
[71] N. L. Rosi, J. Kim, M. Eddaoudi, B. Chen, M. O'Keeffe, O. M. Yaghi, *J. Am. Chem. Soc.* **2005**, *127*, 1504.
[72] H. Deng, S. Grunder, K. E. Cordova, C. Valente, H. Furukawa, M. Hmadeh, F. Gándara, A. C. Whalley, Z. Liu, S. Asahina, H. Kazumori, M. O'Keeffe, O. Terasaki, J. F. Stoddart, O. M. Yaghi, *Science* **2012**, *336*, 1018.
[73] J. Wang, Y. Fan, H. W. Lee, C. Yi, C. Cheng, X. Zhao, M. Yang, *ACS Appl. Nano Mater.* **2018**, *1*, 3747.
[74] J. Liu, J. Zheng, D. Barpaga, S. Sabale, B. Arey, M. A. Derewinski, B. P. McGrail, R. K. Motkuri, *Eur. J. Inorg. Chem.* **2018**, *2018*, 885.
[75] J. Hu, Y. Chen, H. Zhang, Z. Chen, *J. Solid State Chem.* **2021**, *294*, 121853.
[76] A. Ö. Yazaydin, R. Q. Snurr, T. H. Park, K. Koh, J. Liu, M. D. LeVan, A. I. Benin, P. Jakubczak, M. Lanuza, D. B. Galloway, J. J. Low, R. R. Willis, *J. Am. Chem. Soc.* **2009**, *131*, 18198.
[77] Y. Liu, H. Kabbour, C. M. Brown, D. A. Neumann, C. C. Ahn, *Langmuir* **2008**, *24*, 4772.
[78] Z. Tan, P. Miao, M. Hagihala, S. Lee, Y. Ishikawa, S. Torii, M. Yonemura, T. Saito, S. Deng, J. Chen, L. He, R. Du, J. Zhang, H. Li, J. Sun, Y. Wang, X. Lin, K. Li, T. Kamiyama, *J. Phys. Chem. Lett.* **2020**, *11*, 6785.
[79] S. Margadonna, K. Prassides, A. N. Fitch, *J. Am. Chem. Soc.* **2004**, *126*, 15390.
[80] R. Roy, D. K. Agrawal, H. A. McKinstry, *Annu. Rev. Mater. Sci.* **1989**, *19*, 59.
[81] T. Suzuki, A. Omote, *J. Am. Ceram. Soc.* **2006**, *89*, 691.
[82] J. Chen, X. Xing, C. Sun, P. Hu, R. Yu, X. Wang, H. Li, *J. Am. Chem. Soc.* **2008**, *130*, 1144.
[83] C.-É. Guillaume, *J. Phys. Theor. Appl.* **1898**, *7*, 262.
[84] T. Kamencek, E. Zojer, *J. Phys. Chem. C* **2021**, *125*, 24728.
[85] E. Grüneisen, *Handbuch der Physik* (Eds: H. Geiger, K. Scheel), 10th ed., Springer, Berlin **1926**.
[86] J. M. Ziman, *Electrons and Phonons: The Theory of Transport Phenomena in Solids*, Oxford University Press, Oxford **2001**.
[87] S. Baroni, S. de Gironcoli, A. Dal Corso, P. Giannozzi, *Rev. Mod. Phys.* **2001**, *73*, 515.
[88] J. P. Perdew, K. Burke, M. Ernzerhof, *Phys. Rev. Lett.* **1996**, *77*, 3865.
[89] J. P. Perdew, K. Burke, M. Ernzerhof, *Phys. Rev. Lett.* **1997**, *78*, 1396.
[90] J. P. Perdew, A. Ruzsinszky, G. I. Csonka, O. A. Vydrov, G. E. Scuseria, L. A. Constantin, X. Zhou, K. Burke, *Phys. Rev. Lett.* **2008**, *100*, 136406.
[91] J. P. Perdew, A. Ruzsinszky, G. I. Csonka, O. A. Vydrov, G. E. Scuseria, L. A. Constantin, X. Zhou, K. Burke, *Phys. Rev. Lett.* **2009**, *102*, 39902.
[92] P. D. C. C. Dietzel, R. Blom, H. Fjellvåg, *Eur. J. Inorg. Chem.* **2008**, *2008*, 3624.
[93] P. D. C. C. Dietzel, Y. Morita, R. Blom, H. Fjellvåg, *Angew. Chem., Int. Ed.* **2005**, *44*, 6354.
[94] Z. Zhang, Y. Xiao, M. Cui, J. Tang, Z. Fei, Q. Liu, X. Chen, X. Qiao, *Dalton Trans.* **2019**, *48*, 14971.
[95] S. Bhattacharjee, J.-S. Choi, S.-T. Yang, S. B. Choi, J. Kim, W.-S. Ahn, *J. Nanosci. Nanotechnol.* **2010**, *10*, 135.
[96] R. Sanz, F. Martínez, G. Orcajo, L. Wojtas, D. Briones, *Dalton Trans.* **2013**, *42*, 2392.
[97] W. Zhou, H. Wu, T. Yildirim, *J. Am. Chem. Soc.* **2008**, *130*, 15268.

[98] L. J. Wang, H. Deng, H. Furukawa, F. Gándara, K. E. Cordova, D. Peri, O. M. Yaghi, *Inorg. Chem.* **2014**, *53*, 5881.
[99] L. Sun, T. Miyakai, S. Seki, M. Dincă, *J. Am. Chem. Soc.* **2013**, *135*, 8185.
[100] T. G. Glover, G. W. Peterson, B. J. Schindler, D. Britt, O. Yaghi, *Chem. Eng. Sci.* **2011**, *66*, 163.
[101] W. von der Linden, V. Dose, U. von Toussaint, *Bayesian Probability Theory: Applications in the Physical Sciences*, Cambridge University Press, Cambridge **2014**.
[102] P. Hohenberg, W. Kohn, *Phys. Rev.* **1964**, *136*, B864.
[103] W. Kohn, L. J. Sham, *Phys. Rev.* **1965**, *140*, A1133.
[104] G. Kresse, J. Hafner, *Phys. Rev. B* **1993**, *47*, 558.
[105] G. Kresse, J. Hafner, *Phys. Rev. B* **1994**, *49*, 14251.
[106] G. Kresse, J. Furthmüller, *Phys. Rev. B* **1996**, *54*, 11169.
[107] G. Kresse, J. Furthmüller, *Comput. Mater. Sci.* **1996**, *6*, 15.
[108] S. Grimme, J. Antony, S. Ehrlich, H. Krieg, *J. Chem. Phys.* **2010**, *132*, 154104.
[109] S. Grimme, S. Ehrlich, L. Goerigk, *J. Comput. Chem.* **2011**, *32*, 1456.
[110] G. I. Csonka, J. P. Perdew, A. Ruzsinszky, P. H. T. Philipsen, S. Lebègue, J. Paier, O. A. Vydrov, J. G. Ángyán, *Phys. Rev. B: Condens. Matter Mater. Phys.* **2009**, *79*, 155107.
[111] J. M. Skelton, D. Tiana, S. C. Parker, A. Togo, I. Tanaka, A. Walsh, *J. Chem. Phys.* **2015**, *143*, 064710.
[112] P. F. Weck, E. Kim, J. A. Greathouse, M. E. Gordon, C. R. Bryan, *Chem. Phys. Lett.* **2018**, *698*, 195.
[113] A. Togo, I. Tanaka, *Scr. Mater.* **2015**, *108*, 1.
[114] A. Stukowski, *Modell. Simul. Mater. Sci. Eng.* **2010**, *18*, 015012.
[115] R. Gross, A. Marx, *Festkörperphysik*, Oldenbourg Wissenschaftsverlag, Munich **2012**.
[116] C. Kittel, *Introduction to Solid State Physics*, Wiley, New York **2004**.
[117] W. Nolting, *Grundkurs Theoretische Physik 6 – Statistische Physik*, 7th ed., Springer Spektrum, Berlin **2014**.
[118] F. Birch, *Phys. Rev.* **1947**, *71*, 809.
[119] F. D. Murnaghan, *Am. J. Math.* **1937**, *59*, 235.
[120] P. Vinet, J. R. Smith, J. Ferrante, J. H. Rose, *Phys. Rev. B* **1987**, *35*, 1945.
[121] T. Katsura, Y. Tange, *Minerals* **2019**, *9*, 745.
[122] K. Latimer, S. Dwaraknath, K. Mathew, D. Winston, K. A. Persson, *npj Comput. Mater.* **2018**, *4*, 40.
[123] J. George, R. Wang, U. Englert, R. Dronskowski, *J. Chem. Phys.* **2017**, *147*, 074112.
[124] D. Holec, N. Abdoshahi, S. Mayer, H. Clemens, *Materials* **2019**, *12*, 1292.
[125] C. R. Harris, K. J. Millman, S. J. van der Walt, R. Gommers, P. Virtanen, D. Cournapeau, E. Wieser, J. Taylor, S. Berg, N. J. Smith, R. Kern, M. Picus, S. Hoyer, M. H. van Kerkwijk, M. Brett, A. Haldane, J. del Río, M. Wiebe, P. Peterson, P. Gérard-Marchant, K. Sheppard, T. Reddy, W. Weckesser, H. Abbasi, C. Gohlke, T. E. Oliphant, *Nature* **2020**, *585*, 357.
[126] P. Virtanen, R. Gommers, T. E. Oliphant, M. Haberland, T. Reddy, D. Cournapeau, E. Burovski, P. Peterson, W. Weckesser, J. Bright, S. J. van der Walt, M. Brett, J. Wilson, K. J. Millman, N. Mayorov, A. R. J. Nelson, E. Jones, R. Kern, E. Larson, C. J. Carey, I. Polat, Y. Feng, E. W. Moore, J. VanderPlas, D. Laxalde, J. Perktold, R. Cimrman, I. Henriksen, E. A. Quintero, C. R. Harris, et al., *SciPy 1.0 Contributors, Nat. Methods* **2020**, *17*, 261.
[127] F. Pedregosa, G. Varoquaux, A. Gramfort, V. Michel, B. Thirion, O. Grisel, M. Blondel, P. Prettenhofer, R. Weiss, V. Dubourg, J. Vanderplas, A. Passos, D. Cournapeau, M. Brucher, M. Perrot, E. Duchesnay, *J. Mach. Learn. Res.* **2011**, *12*, 2825.
[128] D. C. Wallace, H. Callen, *Am. J. Phys.* **1972**, *40*, 1718.
[129] R. J. Angel, M. Murri, B. Mihailova, M. Alvaro, *Z. Kristallogr. Cryst. Mater.* **2019**, *234*, 129.
[130] J. K. Bristow, J. M. Skelton, K. L. Svane, A. Walsh, J. D. Gale, *Phys. Chem. Chem. Phys.* **2016**, *18*, 29316.
[131] A. P. Giddy, M. T. Dove, G. S. Pawley, V. Heine, *Acta Crystallogr., Sect. A: Found. Crystallogr.* **1993**, *49*, 697.
[132] A. K. A. Pryde, K. D. Hammonds, M. T. Dove, V. Heine, J. D. Gale, M. C. Warren, *J. Phys.: Condens. Matter* **1996**, *8*, 10973.
[133] M. G. Tucker, A. L. Goodwin, M. T. Dove, D. A. Keen, S. A. Wells, J. S. O. Evans, *Phys. Rev. Lett.* **2005**, *95*, 8.
[134] A. L. Goodwin, *Phys. Rev. B: Condens. Matter Mater. Phys.* **2006**, *74*, 134302.
[135] G. D. Barrera, J. A. O. O. Bruno, T. H. K. K. Barron, N. L. Allan, *J. Phys.: Condens. Matter* **2005**, *17*, R217.